Early whole-body mutant huntingtin lowering preserves proteins and lipids important for synapse function and white matter maintenance in the LacQ140 mouse model

Ellen Sapp*‡, Kai Shing*‡, Adel Boudi*, Sophia Liu*, Connor Seeley*, Deanna Marchionini**, Marian DiFiglia*, and Kimberly B. Kegel-Gleason*

‡These authors contributed equally.

*Department of Neurology, Massachusetts General Hospital, Charlestown, MA 02129

**CHDI Management/CHDI Foundation, New York, NY 10001

Corresponding Author: Kimberly B. Kegel-Gleason

Address: 114 16th Street, Room 2001

MassGeneral Institute for Neurodegeneration (MIND)

Charlestown, MA 02129

Phone: 617-724-8754

Email: kegel@helix.mgh.harvard.edu

Running title: Huntingtin lowering delays phenotypes

Abstract

Lowering mutant huntingtin (m*HTT*) transcription is a promising approach to treat Huntington's disease (HD). Using a m*Htt*-inducible mouse model we analyzed m*Htt* lowering initiated at different ages and sustained for different time-periods. mHTT protein in cytoplasmic and synaptic compartments of the caudate putamen, which is most affected in HD, was reduced 38-52%. Little or no lowering of mHTT occurred in nuclear and perinuclear regions where aggregates formed at 12 months of age. m*Htt* transcript repression partially or fully preserved select striatal proteins (SCN4B, PDE10A). Total lipids in striatum were reduced in LacQ140 mice at 9 months and preserved by early partial m*Htt* lowering. The reduction in total lipids was due in part to reductions in subclasses of ceramide (Cer), sphingomyelin (SM), and monogalactosyl diglyceride (MGDG), which are known to be important for white matter structure and function. Lipid subclasses—phosphatidylinositol (PI), phosphatidylserine (PS), and bismethyl phosphatidic acid (BisMePA)—were also changed in LacQ140 mice. Levels of all subclasses other than ceramide were preserved by early m*Htt* lowering. Our findings suggest that early and sustained reduction in m*Htt* can prevent changes in levels of select striatal proteins and most lipids but a misfolded, degradation-resistant form of mHTT hampers some benefits in the long term.

Introduction

Huntington's disease (HD) is a heritable neurodegenerative disease caused by a CAG expansion in the huntingtin (*HTT*) gene. The protein product, huntingtin (HTT), is ubiquitously expressed but enriched in neurons (DiFiglia et al., 1995;Sharp et al., 1995) and has been implicated in numerous molecular functions including vesicle trafficking, autophagy, transcription and DNA repair (Reviewed by (Caviston and Holzbaur, 2009;Saudou and Humbert, 2016;Gao et al., 2019)). HTT has also been shown to have essential functions during development (Duyao et al., 1995;Nasir et al., 1995;Zeitlin et al., 1995;O'Kusky et al., 1999;McKinstry et al., 2014;Barron et al., 2021). The CAG-repeat expansion encodes a polyglutamine expansion in HTT, which causes protein accumulation and aggregation and has pleiomorphic effects that contribute to HD pathology ranging from mitochondrial dysfunction, transcriptional defects, cholesterol mishandling, altered palmitoylation, and metabolic changes from altered signaling in the hypothalamus (Petersen and Bjorkqvist, 2006;Nopoulos, 2016).

HTT transcription lowering strategies have become central to HD translational studies (reviewed by (Tabrizi et al., 2019)). Interventional trials have targeted total *HTT* (that is, normal and mutant *HTT*) using antisense oligonucleotides (ASOs) (reviewed by (Barron et al., 2021)) or *HTT* pre-mRNA using an oral drug, branaplam (LMI070) (Keller et al., 2022). In animal models (mice, sheep, and nonhuman primates), additional strategies of gene therapy using transcriptional repressors to target expression from the mutant allele (Zeitler et al., 2019) and modified interfering RNAs (RNAi) (Alterman et al., 2019) or AAV expressing microRNAs (miRNAs) or short hairpin RNAs (shRNAs) (McBride et al., 2011;Keeler et al., 2016) to target RNA levels are actively being pursued (Rodriguez-Lebron et al., 2005;DiFiglia et al., 2007;Boudreau et al., 2009;Drouet et al., 2009;Kordasiewicz et al., 2012;Stanek et al., 2013;Stanek et al., 2014;Datson et al., 2017;Zeitler et al., 2019).

Although lowering total *HTT* in humans was hoped to be generally safe (Leavitt et al., 2020), insufficient evidence currently exists to make this conclusion. There is support for selective lowering of m*HTT* based on data in mice that show loss of wild type (WT) *HTT* may affect neuronal function including synaptic connectivity (Dragatsis et al., 2000;McKinstry et al., 2014;Mehler et al., 2019;Barron et al., 2021).

Proteins known to change with HD progression may serve as useful readouts for investigating the efficacy of HTT lowering. For instance, DARPP32 is enriched in striatal projection neurons and is progressively reduced in HD patient postmortem brain (Bibb et al., 2000) and in mouse HD models (Menalled et al., 2003;Skotte et al., 2018;Sapp et al., 2020). The cAMP phosphodiesterase PDE10A is reduced early and sustainably in HD striatum measured both by western blot and mass spectrometry (Skotte et al., 2018;Zeitler et al., 2019;Sapp et al., 2020) or ligand binding (Zeitler et al., 2019). Microarray analysis in neurons derived from human stem cells (Mehta et al., 2018), mass spectrometry and western blot analyses in striatal synaptosomes (Sapp et al., 2020) and immunofluorescence (IF) studies in mouse (Oyama et al., 2006) showed SCN4B is lowered in HD models. ATP5A protein levels are altered in numerous mass spectrometry studies (McQuade et al., 2014;Langfelder et al., 2016;Agrawal and Fox, 2019;Sapp et al., 2020). Some lipids are altered by m*Htt* expression (Kegel-Gleason, 2013;Vodicka et al., 2015;Iuliano et al., 2021) and might be useful readouts for evaluating effects of m*HTT* lowering or lead to discovery of new biomarkers.

The effects of lowering total *Htt* or m*Htt* alone on striatal proteins and behavioral and psychiatric measures have been investigated in HD mouse models after delivery of reagents to the striatum or lateral ventricle (Southwell et al., 2018;Zeitler et al., 2019). Biomarkers (mHTT levels and aggregation) that are responsive to total or m*Htt* lowering have been investigated in HD mouse models (Southwell et al., 2015;Bertoglio et al., 2022;Caron et al., 2022). However, the impact of lowering m*Htt* on lipids has not been examined. Here we used the inducible HD knock-in mouse model, LacQ140—in which the expression of m*Htt* is regulated by adding or withdrawing the lactose analog isopropyl b-D-1-thiogalactopyranoside (IPTG) in their drinking water, using an established *Lac* operator/repressor system (Cronin et al., 2001;Scrable, 2002;Coffey et al., 2020;Marchionini et al., 2022)—that allowed us to study the effects of m*Htt* lowering for different time periods on proteins and lipids known to be affected in HD models. We also tracked changes in levels of soluble and aggregated mHTT protein in different subcellular compartments. The results show that early and

sustained reduction in m*Htt* in this HD mouse model can delay select protein changes and prevent numerous lipid derangements but some aggregated mHTT persists.

Results

Time course of mHTT protein lowering with regulated transcriptional repression using LacQ140 mouse striatum

We used the inducible HD knock-in mouse model, LacQ140, in which the expression of m*Htt* throughout the body was regulated by adding or withdrawing the lactose analog isopropyl b-D-1-thiogalactopyranoside (IPTG) in drinking water using an established *Lac* operator/repressor system (Scrable, 2002;Coffey et al., 2020;Marchionini et al., 2022). We used the model to lower m*Htt* from conception, starting at 2 or 8 months of age. To control for effects of IPTG, WT mice also received IPTG treatment over their lifetime. The striatum was examined at 6, 9 and 12 months of age (**Figure 1**).

To determine effects of m*Htt* transcript repression on levels of mHTT and other proteins, we used an automated capillary immunoassay (Wes, Protein Simple, San Jose, CA) and SDS-PAGE and western blot analysis. HTT and mHTT were detected by capillary immunoassay using anti-HTT antibody Ab1 and anti-polyglutamine (polyQ) antibody MW1 (**Figure 2**) and by western blot using anti-HTT antibody EPR5526, and anti-mHTT antibody PHP3 which recognizes an altered conformer of polyproline in mHTT (Ko et al., 2018) (**Supplementary Figure 1**).

In the 6-months-old mice, significant lowering of mHTT detected with Ab1, MW1, and PHP3 occurred in LacQ140_A (35-47%) and LacQ140_2M (38-42%) mice compared to LacQ140 mice (**Figure 2a, Supplementary Figure 1a** and **Supplementary Table 1**). Although EPR5526 recognizes both WT and mHTT, no significant lowering of mHTT protein was measured with m*Htt* gene repression using this antibody (**Supplementary Figure 1a**).

At 9 months, significant lowering of mHTT was detected with antibodies Ab1, MW1, and PHP3 in LacQ140_A (43-52%) and LacQ140_2M (42-46%) mice compared to LacQ140 mice (**Figure 2b, Supplementary Figure 1b** and **Supplementary Table 1**). Anti-HTT antibody EPR5526 at this timepoint showed a significant reduction in mHTT but the degree of change was less than that observed with the other three antibodies: LacQ140_A (24%) and LacQ140_2M (30%) compared to LacQ140 mice.

In the 12-month mice, mHTT was significantly reduced in LacQ140_A (51%) mice compared to LacQ140 mice (**Figure 2c, Supplementary Figure 1c** and **Supplementary Table 1**). This was observed in the capillary immunoassay using antibody Ab1 but not with antibodies MW1, EPR5526, or PHP3. m*Htt* repression in the LacQ140_2M and LacQ140_8M mice yielded no significant reduction of mHTT protein levels compared to LacQ140 mice.

These results show that systemic regulated repression of m*Htt* transcription in LacQ140 mice results in partial lowering of mHTT protein levels in the striatum (38-52%), but a soluble form of mHTT remains.

Effects of m*Htt* lowering on its distribution in different subcellular cytoplasmic compartments

We next looked at the effects of m*Htt* repression on its protein levels in different subcellular compartments. Density gradient fractionation and ultracentrifugation for subcellular fractionation of cytoplasmic components was performed as shown in **Supplementary Figure 2a**. The schematic in **Supplementary Figure 2b** indicates representative proteins that are enriched in different cytoplasmic compartments. In the 6-month mice, equal volumes of all fractions were analyzed for HTT levels by SDS-PAGE and western blot in one set of mice to determine which fractions had HTT signal detected by antibody Ab1 (anti-HTT aa1-17). We found HTT and mHTT in fractions 1-4 and 12-14; there was no measurable HTT signal in some fractions (**Supplementary Figure 2c, right blots**) consistent with our earlier experiments (Velier et al., 1998;Iuliano et al., 2021). We analyzed equal volumes from fractions 1-5 and 12-14 of the remaining 6-months-old LacQ140 mice for all treatment groups (**Supplementary Figure 2c, left blots**). There was no change in the distribution of

WT and mHTT in the fractions between groups consistent with results observed with Q175/Q7 HD mice (**Supplementary Figure 2d**, (Iuliano et al., 2021)). The mHTT/WT HTT ratio was significantly lower in LacQ140_2M mice in fractions 13 and 14 compared to LacQ140 mice (**Figure 3a and b**). Similar results were observed in 12-months-old mice, where there was no change in the distribution of WT and mHTT in the fractions between groups (**Supplementary Figure 2e and f**) and there was lowering of mHTT in fractions 1, 3, 13, and 14 in LacQ140 mice with m*Htt* repression for different periods of time compared to LacQ140 mice (**Figure 3c and d**).

Effects of m*Htt* lowering on its distribution in crude nuclear fractions

In 12-months-old LacQ140 mice, repressing m*Htt* transcription only partially reduced levels of mHTT protein in crude homogenates (**Figure 2c**) even though mHTT was efficiently lowered in the sub cytoplasmic compartments contained in the S1 fraction (**Figure 3d**). We speculated that mHTT may reside in other compartments where it is more resistant to removal by transcript repression. To address this idea, we examined P1 fractions which contain nuclei, ER, large perinuclear structures such as the recycling compartment, some mitochondria and autophagosomes (Kegel et al., 2000). HTT was detected with antibody Ab1 in WT mice (2 alleles worth) and LacQ140 mice (1 allele worth) and mHTT (1 allele worth) in LacQ140 mice at both 6 and 12 months (**Supplementary Figure 3a and b**). Significant lowering of mHTT protein was observed in 6 -months-old LacQ140_A but not LacQ140_2M mice using antibody Ab1 (**Supplementary Figure 3a**). In 12-month mice, repression of the m*Htt* allele at any age or duration failed to lower mHTT protein levels in the P1 fraction (**Supplementary Figure 3b**).

We queried whether forms of mHTT with altered migration with SDS-PAGE could be detected in the P1 fractions using antibody S830 which has been reported by us and others to detect a smear using SDS-PAGE and western blot (Landles et al., 2010;Vodicka et al., 2014). At 12-months, HD mice showed an S830-positive smear above the HTT/mHTT bands which was not lowered in the LacQ140_8M, LacQ140_2M or LacQ140_A mice (**Figure 4a**). Altogether these results show that mHTT in the P1 fraction, which is known to accumulate misfolded species of mHTT with time, is more resistant to mHTT lowering after transcriptional repression.

Mutant HTT aggregation assessed by the filter trap assay: Effects of age and duration of m*Htt* lowering

Gene repression of m*Htt* transcription in LacQ140 mice resulted in lower mHTT protein levels at 6 and 9 months with anti-HTT antibody Ab1 and anti-polyQ antibodies MW1 and PHP3, but only in the LacQ140_A mice at 12 months with Ab1. To determine if mHTT was already aggregated at 12 months and therefore less responsive to mHTT lowering after transcriptional repression, we performed filter trap assays as described in methods.

We observed signal for aggregated mHTT in the R6/2 positive control lysates as expected (**Figure 4b and c**) and HTT-positive insoluble material was detected with S830 antibody in the LacQ140 mouse crude homogenates at 12 months (**Figure 4b**). In contrast, no signal for aggregated mHTT was detected in the LacQ140_A or LacQ140_2M mice, and there was a reduced signal for aggregated mHTT in LacQ140_8M mice compared to LacQ140 mice. These findings indicate accumulation of insoluble mHTT in a time dependent manner and show that lowering m*Htt* early and consistently blocks the accumulation. Lowering at later times results in delay of aggregate accumulation but does not block accumulation of misfolded mHTT completely.

We next assessed levels of aggregated mHTT using the filter trap assay in the P1 fractions of 12-months-old mice since the S830-positive smear observed above the HTT band in these mice by western blot is possible evidence for aggregation. With the S830 antibody, the filter trap assay showed increased aggregated material in the LacQ140 mice compared to WT, LacQ140_8M, LacQ140_2M and LacQ140_A mice (**Figure 4c**). There was more aggregated HTT in the LacQ140_8M mice compared to LacQ140_A and WT mice.

Effects of m*Htt* lowering on levels of GFAP, DARPP32, SCN4B, PDE10A, and ATP5A

Prior studies in different mouse models of HD have shown that levels of some neuronal proteins are altered in the mouse striatum, namely DARPP32, PDE10A, SCN4B, and ATP5A (Gu et al., 1996;Bibb et al., 2000;Oyama et al., 2006;McQuade et al., 2014;Langfelder et al., 2016;Skotte et al., 2018;Agrawal and Fox, 2019;Sapp et al., 2020). To assess levels of these proteins and that of the astrocyte protein glial acidic fibrillary protein (GFAP) in the LacQ140 mice without and with m*Htt* gene repression, crude homogenates from 6, 9, and 12-month-old mice were analyzed by capillary immunoassay or western blot.

In agreement with previous studies in HD mouse models (Skotte et al., 2018;Zeitler et al., 2019;Sapp et al., 2020), striatum from the LacQ140 exhibited a significant reduction in PDE10A at all ages examined. Early m*Htt* lowering starting at 2 months of age statistically preserved PDE10A levels at 6 and 9 months (**Figure 5a and b and Supplementary Table 2**), but the effect was lost by 12 months of age (**Figure 5c and Supplementary Table 2**). SCN4B expression was reduced in the striatum of LacQ140 at 6 and 9 months of age and levels were preserved with early m*Htt* lowering (**Figure 5a and b and Supplementary Table 2**). DARPP32 levels were significantly lower in LacQ140 compared to WT mice at 9 months but not at 6 or 12 months and there were no differences in levels of GFAP and ATP5A between WT and LacQ140 at any age examined (**Supplementary Figure 4**).

Effects of m*Htt* lowering on lipids detected by mass spectrometry

We surveyed for lipid changes in LacQ140 striatum, compared to WT, and the effects of lowering m*Htt* using mass spectrometry (MS) as previously described (Iuliano et al., 2021). For each age, lipids were extracted from crude homogenates of striatum from each treatment group/genotype and analyzed as a set. The total lipids per group were compared. Our MS intensity measurements were relative measurements so only samples processed together can be compared (i.e., by age group). The sum of lipids for each genotype and/or treatment group were reported as a proportion of WT within each age group (**Figure 6a-c**). No changes in total lipid were observed at 6 months or 12 months (**Figure 6 a and c**). However, at 9 months the of LacQ140 mice had significantly lower levels of total lipids compared to WT or to LacQ140_A mice **(Figure 6b**). A heat map and hierarchical clustering of lipid changes by subclass at 9 months revealed two major groups where-in subclasses moved in the same direction even if all weren't statistically significant (**Figure 6d**). The top cluster delimited in blue shows subclasses that decreased in LacQ140 mice compared to WT and were corrected by lowering. In contrast, the cluster marked in red shows subclasses that were increased in LacQ140 mice compared to WT and were corrected by lowering**.** Other subclasses marked in black did not change. Summaries of lipid subclasses and number of species detected for each age group are in **Tables 1, 2, and 3**. Data and graphs for 6-months-old mice subclasses and species can be found in **Supplemental Table 3, Supplementary Figures 5, 6**, **& 11 and Supplemental Prism File A**; 9-months-old mice in **Supplemental Table 4, Supplementary Figures 7, 8**, **& 12 and Supplemental Prism File B**; 12-months-old mice in **Supplemental Table 5, Supplementary Figures 9, 10**, **13, & 14 and Supplemental Prism File C.** An overview of changes in individual species across ages is shown in **Table 4**.

In striatum of LacQ140 mice at 6-months-of-age, no lipid subclasses or species changes survived correction using the Benjamini, Krieger and Yekutieli procedure with a 5% false discovery rate (FDR) of q <0.05, n=36 subclasses (**Table 1**) and n=800 species (**Supplementary Table 3**), although the glycerophospholipid subclass phosphatidylinositol (PI) was increased in LacQ140 compared to WT littermate controls by one-way ANOVA (**Supplementary Figure 5**), as were individual species of PI and phosphatidylserine (PS) (**Supplementary Table 3 and Supplementary Figure 11 and Prism File A**).

In striatum of LacQ140 mice, increases in two glycerophospholipid subclasses, PS and PI, were measured at 9 months (**Table 2 and Figure 7a and b**). A significant reduction in bismethyl phosphatidic acid (BisMePA) also occurred (**Table 2 and Figure 7c**). We measured significant reductions in sphingolipid subclasses sphingomyelin (SM) and Ceramide (Cer) (**Table 2; Figure 7e and f**), and the low abundance lipid monogalactosyl diglyceride (MGDG) (**Table 2**; **Figure 7g**) in LacQ140 mice, compared to WT. All subclasses with changes between WT and LacQ140 significant by one-way ANOVA

also had q values<0.05 using the Benjamini, Krieger and Yekutieli procedure (n=24 subclasses) (**Table 2**). Heat maps show that the changes at the subclass level were due to large numbers of individual lipid species changing within each subclass even if each species is not significantly different (**Figure 7d and h**).

Lowering m*Htt* from 0-9 months (LacQ140_A) corrected levels of all these lipids towards WT levels, except Cer although even Cer trended towards WT levels. Lowering m*Htt* from 2-9 months (LacQ140_2M) was sufficient to correct SM and MGDG to WT levels (**Figure 7 e, g).** Changes among other treatment groups occurred for phosphatidylethanolamine (PE), triacylglycerol (TG) and Hexosylceramides (Hex1Cer) but only TG had a q<0.05 (**Table 2 and Supplementary Figure 8**). Fourteen species with q<0.05 were significantly changed between WT and LacQ140 and all 14 showed improvement with partial m*Htt* lowering at 9 months (n=632) (**Supplementary Table 4, Supplementary Figure 12, and Supplementary File Prism File B**). This included 2 species of PI and 3 species of PS which were all significantly increased in LacQ140 mice versus WT. Three species of Hex1Cer, 1 species of SM and 1 species of MGDG were decreased in LacQ140 mice compared to WT and recovered with lowering.

In striatum of LacQ140 mice at 12 months, no significant differences at the subclass level were found compared to WT by one-way ANOVA (**Table 3 and Supplementary Figures 9 and 10 and Prism File C**) although 29 subclasses were measured. At the individual lipid species level, 26 were changed between WT and LacQ140 mice with q<0.05 (n=735) (**Supplementary Table 5 and Supplementary File Prism File C**). The only lipid species which was increased in LacQ140 mice at 12 months compared to WT and had levels restored by m*Htt* lowering was Ceramide Phosphate (**Supplementary Fig. 14**). Of note, nine species of TGs, eight of which contain oleic acid (18:1), were reduced in LacQ140 mice compared to WT (**Supplementary Fig. 13**) and did not correct with lowering.

To determine if any of the lipid changes could be explained by altered transcription of genes regulating lipid-related metabolic pathways, we re-examined the RNAseq data that was generated in the previous study of the LacQ140 mice at 6 and 12 months (Marchionini et al., 2022). Differentially expressed genes (DEGs) were manually curated for genes which could affect levels of PI, PS, sphingolipids and glycerolipids. Phosphatidylserine synthases (*PSS1* and *PSS2*) which catalyze creation of PS (Kim et al., 2014) were not reported as changed in the LacQ140 mice. Similarly, the rate limiting enzymes for PI synthesis, CDP-diacylgycerol synthases (*CDS1* and *CDS2*) (Blunsom and Cockcroft, 2020) also were unchanged. However, numerous gene changes (both up and down) for LacQ140 striatum, compared to WT, occurred for enzymes that could impact PI levels directly or by metabolizing PI-phosphates (PIPs) at 6 and 12 months (**Supplementary Tables 6 and 7 and Supplementary Figure 15 a and b**). The same was true for sphingolipids, although most DEGs regulating sphingolipids were down at both 6 and 12 months (**Supplementary Tables 6 and 7 and Supplementary Figure 15c and d**). Of note, one subunit of the rate limiting enzyme for synthesis of sphingolipids, called serine palmitoyl transferase small subunit B (*SPTSSB*), was down at 6 months. UDP-galactose-ceramide galactosyltransferase (*UGT8A*) which catalyze the formation of GalCer (Hex1Cer) from Cer was down at both 6 and 12 months in the LacQ140 mice (**Supplementary Tables 6 and 7 and Supplementary Figure 15c and d).** Fatty acid 2-hydroxylase (*FA2H*), in which mutations cause hereditary spastic paraplegia 35 (Edvardson et al., 2008; Hardt et al., 2020), was decreased in the LacQ140 mice at the 6- and 12-month timepoints (**Supplementary Tables 6 and 7 and Supplementary Figure 15c and d**). For glycerolipids, the only 2 known enzymes that catalyze TG synthesis were changed: diacylglycerol acyl transferase (*DGAT*)2 was down at 12 months where-as *DGAT*1 was up at 12 months (**Supplementary Tables 6 and 7 and Supplementary Figure 15e and f**).

Lipid changes might be explained by altered cellular composition of tissue. To address this possibility, we also examined the published RNAseq data in LacQ140 mice (GEO GSE156236) for changes in transcript levels for cellular markers. No change in mRNA expression levels for the microglial markers Iba1 and CD68, or for the reactive astrocyte marker GFAP were reported that might indicate upregulation of these cell types could account for the lipid changes. However, we did find reduced transcripts of genes important for oligodendrocyte development and myelin maintenance (**Supplementary Tables 6 and Supplementary Figure 15g and h**). For instance, proteolipid protein 1 (*PLP1*) in which mutations cause spastic paraplegia 2 and Claudin11 (*CLDN11*) were down at both 6 and 12 months. The transcription factor, Tcf712 was also down at 6 months, as was Myelin basic protein (*MBP*) and myelin and lymphocyte protein (*MAL)*. At 12 months the

mature oligodendrocyte marker myelin associated oligodendrocyte basic protein (*MOBP)* was down, and in contrast the immature oligodendrocyte marker Olig1 was up.

In summary, numerous changes in lipids occur in LacQ140 striatum that can be aided by m*Htt* lowering. Some of our lipidomic findings might be explained in part by altered transcription in LacQ140 mice.

Discussion

Here we used the LacQ140 inducible HD mouse model to initiate whole body m*Htt* reduction at different ages and evaluate effects on proteins and lipids. Lowering mHTT protein by 38-52% in the LacQ140 caudate-putamen, starting from conception up to 12 months of age, was sufficient to prevent m*Htt* induced changes in the levels of some proteins and most lipids. However, a resistant soluble species of the protein detected in older mice limited long term benefit of m*Htt* lowering.

We identified specific forms of mHTT protein that were resistant to m*Htt* lowering, as detected by specific HTT antibodies. These resistant forms of mHTT identified by immunoblot may correspond to mHTT aggregates or foci found to be resistant to lowering in LacQ140 mice using MSD and immunofluorescence methods (Marchionini et al., 2022). Others have described aggregated and soluble forms of mHTT that resist degradation in specific cellular compartments (Diaz-Hernandez et al., 2005;Zeitler et al., 2019;Fox et al., 2020). In the LacQ140 striatum, the SDS-soluble degradation-resistant form of full-length mHTT, detected by us using antibody S830, that resides in a perinuclear or nuclear compartment might be part of the "juxtanuclear quality control compartment (JUNQ)" described by Frydman and colleagues (Kaganovich et al., 2008). Altogether, these results highlight the importance of using multiple antibodies and methods to track mHTT resistant proteoforms (Sapp et al., 2020) which interact with diverse targets in cells (Wanker et al., 2019). Targeting these resistant fractions of misfolded mHTT by a chaperone activity to aid in its degradation may be beneficial in combination with gene therapy *HTT* lowering strategies.

We found that early, continuous partial lowering of mHTT protein for up to 12 months fully or partially preserved PDE10A and SCN4B protein levels. These data agree with other results showing preservation *Pde10a* mRNA in the LacQ140 model after early m*Htt* lowering (Marchionini et al., 2022) and preservation of the Pde10a PET signal in the Q175 model after striatal injection of AAV-HTT-ZFP (Zeitler et al., 2019). However, our data indicate that the time points chosen for post-treatment analysis are important and changes do not follow a linear neurodegenerative trajectory in mice. For instance, the greatest number of changes in LacQ140 mice occurred at 9 months, not at 12 months. Similarly, Langfelder et al. found a greater number of differentially expressed genes at 6 months compared to 10 months in zQ175 mice (Langfelder et al., 2016). This suggests that in mouse brain, adverse responses to mHTT may oscillate or go through waves of degeneration and regeneration. Therefore, to appreciate any benefits afforded by m*Htt* lowering, frequent or continuous monitoring should be conducted.

In this study, mass spectrometry of lipids identified numerous alterations in LacQ140 striatum, many of which were prevented with modest m*Htt* lowering. To our surprise, lipidomic analysis showed that LacQ140 mice had increased levels in species of the glycerophospholipid PI and PS starting at 6 months and progressing to a significant change in the PI and PS subclass level at 9 months. PI is the precursor for PIPs which are important for protein kinase c (PKC) signaling at the synapse via generation of DG (DAG) and IP3 by phospholipase C (Berridge, 2016). PIPs also act as important docking and activating molecules for membrane associated proteins, including HTT (Kegel et al., 2009a). Proteomics in Q140 synaptosomes revealed changes in proteins that regulate PI levels including PKC signaling and PIP2 hydrolysis, two isoforms of DGKs, and in one of the rate-limiting enzymes in PI synthesis (CDS2) (Sapp et al., 2020), all of which impact PI levels (Blunsom and Cockcroft, 2020). Transcriptomics on the LacQ140 mice also showed a plethora of DEGs for enzymes that impact PI and PIPs (Marchionini et al., 2022) and our manual curation of that data is in Supplementary Tables 6 and 7. PS is an abundant anionic glycerophospholipid necessary for activation of several ion channels (Hirt and Leist, 2003), neurotransmitter vesicle fusion, regulation of AMPA signaling, and coordination of PKC, Raf-1 and AKT signaling (Kim et al., 2014). Normally found on the inner leaflet of the plasma membrane, PS can be externalized by apoptotic cells to

signal for removal (Williamson and Schlegel, 2002) and in neuronal synapses externalized PS signals to microglia for synaptic pruning (Scott-Hewitt et al., 2020). Microglial activation occurs in HD post-mortem brain (Sapp et al., 2001) and increased pruning by microglia may contribute to synaptic loss in R6/2 HD striatum (Savage et al., 2020) and in zQ175 and BACHD mice as well as HD brain (Wilton et al., 2021). An overall increase in PS could inadvertently mark synapses for engulfment by microglia. The ratio of PS to PE impacts autophagy (Polyansky et al., 2022) which may in turn impair mHTT removal (Qin et al., 2003;Yamamoto et al., 2006). Both PI and PS are abundant in astrocytes as well as neurons (Fitzner et al., 2020), so it is unclear which cell type(s) is producing the changes in these lipids. We cannot rule out that lipid changes are due to altered cellular composition of the brain.

The intracellular location of HTT positions it to affect lipids in membranes. HTT normally associates with membranes where it interacts directly with lipid bilayers. Polyglutamine expansion in HTT altered its interaction with synthetic lipid vesicles containing PIPs (Kegel et al., 2009a) and changed intracellular membrane targeting (Atwal et al., 2007). mHTT fragments penetrate and disrupt synthetic bilayers (Kegel et al., 2009b). It is unclear whether changes in myelin-related lipids are a primary site of pathology or a consequence of Wallerian degeneration of cortical-striatal axons with primary pathology in the neuron. Interestingly, the presence of SM increased permeabilization of monolayers by mHTT (Chaibva et al., 2018), suggesting mHTT may have particular effects on myelin lipids. Furthermore, mHTT was localized within myelin sheaths using immunogold EM in 9-month-old Q175 striatum (Ko et al., 2018). There is evidence that mHTT can be secreted by neurons in culture and in brain as a soluble free form (Caron et al., 2021). We speculate that mHTT could insert directly into myelin bilayers to disrupt myelin architecture.

Changes in white matter detected through imaging are one of the first signs of disease in people with HD (PwHD) (Rosas et al., 2006;Paulsen et al., 2008;Paulsen, 2009;Hobbs et al., 2010;Di Paola et al., 2012;Phillips et al., 2013;Singh et al., 2013;Matsui et al., 2015;Odish et al., 2015;Poudel et al., 2015;Faria et al., 2016;Bourbon-Teles et al., 2019;Tereshchenko et al., 2019;Sweidan et al., 2020;Oh et al., 2021). Morphometric studies of postmortem HD brain showed reduced cross-sectional area of white matter in addition to gray matter atrophy (de la Monte et al., 1988;Vonsattel and DiFiglia, 1998). Lipid content in HD post-mortem brain tissue reported a dramatic shift in the profile of various sphingolipids including Cer, SM, hexosylceramides, and sulfatides (Phillips et al., 2022). Here, we demonstrate in the striatum of 9-months-old LacQ140 mice significant reductions (compared to WT mice) of relative levels of total lipids and the lipid subclasses SM and Cer, and individual species of Hex1Cer, all important for myelin (O'Brien and Sampson, 1965). Our data are in alignment with data from R6/1 mice showing changes in cerebroside and sulfatide levels (Desplats et al., 2007), from the R6/2 mouse model showing reductions in components of the sphingolipid biosynthesis pathway (Di Pardo et al., 2017), and findings in a transgenic sheep model OVT73 similarly showing decreased levels of numerous species of SM (Skene et al., 2017). A salient finding was a profound reduction in LacQ140 striatum of the low abundance signaling lipid MGDG, which regulates oligodendrocyte differentiation (Inoue et al., 1971). MGDG is considered a marker of myelination and stimulates PKC-alpha activity in oligodendrocytes to support process formation (Schmidt-Schultz and Althaus, 1994). We previously reported reduced levels of MGDG in subcellular fractions of Q175/Q7 HD striatum at 2 and 6 months (Iuliano et al., 2021). Crucially, in LacQ140 mice, lowering m*Htt* improved loss of SM and MGDG suggesting protection against white matter pathology.

Observing white matter changes in animal models has been challenging. White matter loss was reported in R6/1 mice (Rattray et al., 2013) and changes in myelination have been described in Yac128 (Teo et al., 2016;Teo et al., 2019) and HdhQ250 mice (Jin et al., 2015), but experiments designed to look for white matter changes in the Q150 HD mouse model showed brain atrophy but no white matter abnormalities (Steventon et al., 2016). A recent imaging study of OVT73 sheep brain reported changes in diffusivity in the internal capsule at 9-10 years, suggesting changes in white matter (Taghian et al., 2022). Our biochemical experiments here show that mHTT effects on striatal lipid homeostasis in HD mouse models are complex. We and others have reported lipidomic and metabolomic studies on knock-in Q140/Q140 HD mice at single time points (Vodicka et al., 2015) and Q111 HD mice (Carroll et al., 2015) but did not observe loss of lipids important for white matter. Curiously, the lipid differences in LacQ140 mice measured at 9 months disappeared at 12 months suggesting that, even in the absence of m*Htt* lowering, the mouse brain insulted with mHTT attempts to heal itself and succeeds at some level. Consistent with our lipidomic findings, a longitudinal imaging study

over 18 months showed transient changes in diffusivity /FA of corpus collosum in Q140 mouse brain (Perot et al., 2022). These results echo imaging data from presymptomatic PwHD suggesting attempted remyelination (Phillips et al., 2014). By 12 months, although changes at the lipid subclass level were annulled, a detailed analysis of the individual lipid species comprising these subclasses shows a shift in species within each subclass. The altered composition of subclasses may weaken HD brains or predispose them to further stress. Hence, if HD mouse models undergo a series of degeneration and regeneration cycles, observations at one or two time points may be misleading.

Changes impinging on oligodendrocyte differentiation or survival due to a primary effect of mHTT protein on transcription in the nucleus may account for the lipid changes we observed. RNA transcripts of genes important for oligodendrocyte differentiation and myelin sphingolipid biosynthesis were altered in LacQ140 mice (Marchionini et al., 2022). The transcription factor TCF7L2, which was lower at 6 months in LacQ140 mice, was recently implicated in altered myelin formation in R6/2 and Q175 mice (Benraiss et al., 2022). The basic helix-loop-helix transcription factor *OLIG*1, which was increased at 12 months in LacQ140 mice compared to WT, is important for commitment of cells to CNS oligodendrocyte identity (Dai et al., 2015). Critically, Lim et al. presented evidence showing abnormal oligodendrocyte maturation in multiple HD postmortem brain regions, as well as R6/2 brain, with single cell RNAseq showing changes in OLIG1 and OLIG2 (Lim et al., 2022). Changes in particular enzyme levels that regulate lipid biosynthesis can have dire consequences. Work by others showed that mice deficient in *UGT8A* exhibited abnormal myelin maturation and structure (Bosio et al., 1996;Coetzee et al., 1996). Mutations in the *FA2H* gene cause the leukodystrophy hereditary spastic paraplegia 35 (Edvardson et al., 2008;Hardt et al., 2021). Interestingly, adult *FA2H*-deficient mice have normal oligodendrocyte differentiation with normal appearing myelin that later degenerates showing “splitting of lammelae” by 18 months (Zoller et al., 2008). This is similar to the Ki140CAG mouse model (Perot et al. 2022) where myelin appears to be quite normal into early adulthood, but then may start to degenerate with disease progression. Both *Ugt8a* and *Fa2h* mRNA were lower in the striatum of LacQ140 (GEO GSE156236). Altered levels of myelin transcripts were found in human ESCs differentiated along an oligodendrocyte pathway (Osipovitch et al., 2019) and an epigenic etiology for changes in myelin gene expression in human oligodendrocyte precursors that was blocked by inactivation of m*HTT* allele was described (Ferrari Bardile et al., 2019).

Not all lipid changes were reversed with m*Htt* lowering. Consistent with metabolic defects in HD, here we report reduced levels of species of TG, glycerolipid molecules used for energy storage which can be metabolized by mitochondria, in LacQ140 compared to WT. Of note, reductions in species of TG were not reversed by m*Htt* lowering. Interestingly, the LacQ140 mice exhibited reciprocal changes in the two biosynthetic enzymes DGAT1 and DGAT2 at the transcriptional level (GEO GSE156236), suggesting the ability to store energy may arise in part from this variation.

Conclusions

Collectively, our studies advocate early lowering of m*HTT* for greatest benefit, and in this context modest lowering is sufficient to delay some protein and lipid changes. Furthermore, our work shows readily detectable but transient changes in lipids highly enriched in myelin, consistent with possible white matter damage and regeneration occurring in the LacQ140 mouse model.

Materials and Methods

Animals.

The *LacO*/*LacIR*-regulatable HD mouse model (LacQ140) was generated by crossing the $Htt^{LacQ140/+}$ mouse to the $Tg^{ACTB\text{-}lacI*Scrb}$ mouse as previously described (Cronin et al., 2001;Marchionini et al., 2022). The default state of the LacQ140 mouse is global repression of m*Htt* due to *Lac* Repressor binding to the *Lac* operators. The continuous administration of IPTG starting from E5 interrupts the binding between the *Lac* repressor and operators, resulting in a de-repressed state,

and maximal expression of m*Htt* in LacQ140. All WT mice were $Htt^{LacO+/+}$; b-actin-$LacI^{R}$ tg. Mice were housed at Psychogenics (Paramus, NJ) and all treatments and procedures were conducted with oversight by Psychogenics Institutional Animal Care and Use Committee. Mice were provided with enrichment (envirodry, play tunnels, Bed-o'cobs and plastic bones) and housed uniform for genotype, gender, and treatment. Mice were fed *ad libitum*. The lactose analog IPTG was provided in drinking water (at 10mM) which de-represses the *LacQ140* allele and keeps normal m*Htt* expression. During embryonic development, m*Htt* expression levels were maintained at normal levels by administering IPTG to pregnant dams starting at embryonic day 5 (E5). IPTG was administered never (*mHtt* repressed), always (*mHtt* always expressed) or withdrawn at 2 or 8 months (*mHtt* expressed normally then repressed at 2 or 8 months).

The CAG repeat length range in $Htt^{LacO\text{-}Q140/+}$ mice was 143-157 with average of 148 and median of 148 CAG.

Sample preparation. The striatum from one hemisphere for each mouse was homogenized in 750 µl 10mM HEPES pH7.2, 250mM sucrose, 1uM EDTA + protease inhibitor tablet (Roche Diagnostics GmbH, Mannheim, Germany) + 1mM NaF + 1mM Na3VO4. A 150µl aliquot of this crude homogenate was removed and protein concentration was determined using the Bradford method (BioRad, Hercules, CA). Subcellular fractionation by density gradient ultracentrifugation using Optiprep was performed on remaining 600 µl sample for the 6 and 12 month old mice as previously described (Iuliano et al., 2021).

Capillary immunoassay. Equal amounts of protein from the crude homogenates were analyzed using the automated simple western system, Wes (ProteinSimple, Bio-Techne, San Jose, CA), which utilizes a capillary-based immunoassay. The protocol described in the manual was followed to detect HTT, GFAP and DARPP32 using 0.6 µg of sample. Quantitative analysis of protein levels is done automatically using the Compass for Simple Western Software (ProteinSimple) on electropherogram data. The peak area (using automatic "dropped line" option in software) of each protein of interest was normalized to the peak area of the vinculin loading control. Figures show protein bands similar to traditional western blots using "lane view" option in the Compass software to create a blot-like image from the electropherogram data.

Western blot analysis. Equal amounts of protein from the crude homogenates were analyzed by western blot for levels of HTT and other proteins of interest as previously described (Sapp et al., 2020). Briefly, 10 µg of protein were separated by SDS-PAGE, transferred to nitrocellulose, and probed with primary antibody overnight. Peroxidase labeled secondary antibodies were used with the SuperSignal West Pico Chemiluminescent substrate (ThermoScientific, Rockford, IL, #34580) and digital images were captured with a CCD camera (AlphaInnotech, Bayern, Germany). For western blot analysis of subcellular fractions, equal volumes of each sample (15 µl) were separated by SDS-PAGE. Pixel intensity quantification of the western blot signals on the digital images was determined using ImageJ software (NIH) by manually circling each band and multiplying the area by the average signal intensity. The total signal intensity was normalized to vinculin or GAPDH loading controls.

Antibodies. The following antibodies and dilutions were used in this study: Anti-HTT Ab1 (aa1-17, (DiFiglia et al., 1995)) 1:50 for capillary immunoassay and 1:2000 for western blot; anti-HTT EPR5526 (Abcam, Waltham, MA, ab109115, 1:2000 for western blot); anti-polyQ MW1 (MilliporeSigma, Burlington, MA, MABN2427, 1:50 for capillary immunoassay); anti-polyQ PHP3 (generous gift from Dr. Ali Khoshnan, 1:2000 for western blot); Anti-PDE10A (Abcam, Waltham, MA, #ab177933, 1:2000 for western blot); Anti-DARPP32 (Abcam, #ab40801, 1:2000 for capillary immunoassay); Anti-GFAP (MilliporeSigma, Burlington, MA, AB5804, 1:3000 for capillary immunoassay); Anti-GAPDH (MilliporeSigma, Burlington, MA, #MAB374, 1:10000 for western blot); Anti-Sodium channel subunit beta-4 (Abcam, Waltham, MA, #ab80539, 1:500 for western blot); Anti-vinculin (Sigma, St. Louis, MO, #V9131, 1:5000 for capillary immunoassay, 1:2000 for western blot); Anti-ATP5A (Abcam, Waltham, MA, #ab14748, 1:2000 for western blot); Anti-HTT MW8 (University of Iowa Developmental Studies Hybridoma Bank, 1:1000 for filter trap); Anti-HTT S830 (generous gift from Dr. Gillian Bates, (Landles et al., 2010) 1:8000), HDAC1 (Abcam, Waltham, MA, ab32369-7, 1:4000).

Filter trap assay. Based on protocol described in Weiss et al 2008 (Scherzinger et al., 1997;Weiss et al., 2008), equal protein amounts for each sample (40 µg) were brought up to 50 µl volume with PBS and 50 µl 4% SDS in PBS was added

to each sample to make final concentration 2% SDS. A cellulose acetate membrane was wet in 2% SDS/PBS and placed in dot blot apparatus. The 100 µl samples were added to each well and pulled through the membrane with a vacuum then washed 3 times with 200 µl 2% SDS/PBS. The membrane was removed from the apparatus, washed in Tris buffered saline + 0.1% Tween-20 (TBST) then processed as for western blot using MW8 or S830 antibodies. The total signal intensity of each dot was measured in ImageJ by circling the entire dot and multiplying the area by the average signal intensity minus the background signal from an empty dot.

Statistical analysis. One-way ANOVA with Tukey's multiple comparison test was performed to determine significance between groups. Asterisks on graphs show p values and are described in the figure legends.

Lipid extraction. Lipids were extracted using methyl tert-butyl ether (MTBE) as previously described and analyzed using ion switching and molecular assignment as previously described (Matyash et al., 2008;Breitkopf et al., 2017;Iuliano et al., 2021). Each age group was processed together. Crude homogenates (100 µl) of dissected mouse striatum were transferred into 20 ml glass scintillation vials. 750 µl of HPLC grade methanol was added to each sample, then vials were vortexed. 2.5 ml of MTBE was then added to each sample and incubated on a platform shaker for 1 hour. After incubation, 625 µl of water was added to induce polar and non-polar phase separation. The non-polar lipid containing (upper) phase was collected into a new vial, and the polar (lower) phase was subsequently re-extracted with 1 ml of MTBE/methanol/water (10/3/2.5, v/v/v). Following re-extraction, the lipid containing phases were combined and allowed to dry on a platform shaker, then further dried with nitrogen gas. Extracted lipids were hand delivered to the Beth Israel Deaconess Medical Center Mass Spectrometry Core Facility.

Lipid Annotation. Data for each timepoint was classified by LIPID MAPS category: glycerophospholipids, glycerolipids, sphingolipids, sterol lipids, fatty acyls, and prenol lipids were detected (Liebisch et al., 2020). Each category contains distinct subclasses as annotated below. *Glycerophospholipids:* Phosphatidylcholine (PC), Phosphatidylethanolamine (PE), Phosphatidylserine (PS), Phosphatidylinositol (PI), Methylphosphocholine (MePC), Phosphatidic acid (PA), Bis-methyl phosphatidic acid (BisMePA), Dimethyl phosphatidylethanolamine (dMePE), Phosphatidylgylcerol (PG), Bis-methylphosphatidylserine (BisMePS), Bis-methyl phosphatidyl ethanolamine (BisMePE), Cardiolipin (CL), Phosphatidylethanol (PEt), Biotinyl-phosphoethanolamine (BiotinylPE), Phosphatidylmethanol (PMe), Phosphatidylinositol-bisphosphate (PIP2), Phosphatidylinositol-monophosphate (PIP), Lysophosphatidylcholine (LPC), Lysophosphatidylethanolamine (LPE), Lysophosphatidylserine (LPS), Lysophosphatidylinositol (LPI), Lysophosphophatidylgylcerol (LPG), Lysodimethyl phosphatidyl ethanolamine (LdMePE). *Glycerolipids:* Triglyceride (TG), Monogalactosyldiacylglycerol (MGDG), Monogalactosylmonoacylglycerol (MGMG), Diglyceride (DG), Sulfoquinovosylmonoacylglycerol (SQMG), Sulfoquinovosyldiacylglycerol (SQDG). *Sphingolipids:* Hexosylceramides (Hex1Cer), Simple Glc series (CerG1), Sphingomyelin (SM), Ceramide (Cer), Ceramide phosphate (CerP), Sulfatide (ST), Sphingoid base (So), Sphingomyelin phytosphingosine (phSM), Simple Glc series (CerG2GNAc1), Ceramide phosphorylethanolamine (CerPE), Sphingosine (SPH), Dihexosylceramides (Hex2Cer). *Sterol lipids*: Cholesterol ester (ChE), Zymosterol (ZyE). *Fatty acyls:* Fatty acid (FA), Acyl Carnitine (AcCa). *Prenol lipids:* Coenzyme (Co).

Individual lipid species were annotated according to sum composition of carbons and double bonds in the format Lipid Subclass (total number of carbons: total number of double bonds). If distinct fatty acid chains could be identified, they were annotated separated by an underscore (ex. PC 32:1, or PC (16:0_16:1). Using this approach, we cannot determine the *sn*-1 or *sn*-2 positions of the fatty acid chains. Lipid species within the sphingolipid category contain prefixes 'd' or 't' to denote di-hydroxy or tri-hydroxy bases. For example, SM(d18:1_23:0) contains 2 hydroxyl groups. The Hex1Cer subclass is comprised of both glucosylceramide (GlcCer) and galactosylceramide (GalCer); the orientation of one of the hydroxyl groups in Glc differs from in Gal, and thus cannot be resolved by these methods (Reza et al., 2021). Plasmanyl lipid species (ether linked) are annotated by 'e' and plasmenyl/plasmalogen (vinyl ether linked) lipid species are annotated by 'p' (ex. PC (36:5e) or PE (16:0p_20:4) (Koelmel et al., 2017).

Bioinformatics. Heatmaps and hierarchical clustering were generated using Morpheus from the Broad Institute (Cambridge, MA, https://software.broadinstitute.org/morpheus). Hierarchical clustering was performed across all rows (lipid subclasses) using the one minus Pearson correlation distance metric. Rows determined to be the most similar are merged first to produce clusters, working iteratively to merge rows into clusters. The dendrogram displays the order of clustering with the most similar rows are displayed in closest proximity. Lipid expression values are assigned to colors

based on the minimum (blue, low relative expression) and maximum (red, high relative expression) values for each independent row. Each column represents data from one animal. RNA sequencing data in the LacQ140 mouse model (GEO GSE156236) was manually curated to identify differentially expressed transcripts related to phosphatidylinositol (PI)/ phosphatidylinositol-phosphate (PIP) metabolism, sphingolipid metabolism, glycerolipid metabolism, and myelin or oligodendrocytes. Volcano plots were generated from the DEG list (fold change greater than 20% in either direction with an FDR adjusted p-value<0.05 were considered differentially expressed) using VolcaNoseR software (Goedhart and Luijsterburg, 2020). For plotting purposes, FDR adjusted p-values from the DEG list are -log10 transformed and fold changes are log2 transformed.

Acknowledgements

This work was supported by CHDI Foundation, Inc. and the Dake family fund to MD and KBK-G and NIH 1S10RR023594S10 to MD. The authors would like to acknowledge the Dake family for their support.

Author Contributions

KKG, MDF, and DM conceived experimental plan and wrote manuscript. ES performed protein chemistry analysis and edited manuscript, KS performed all lipidomics and bioinformatics, AB aided in the experimental plan and edited manuscript, CS and SL performed subcellular fractionations.

Competing interests

KBK-G spouse owns less than 0.1% stock in the following companies: Advanced Microdevices, Aveo Pharmaceuticals, Inc, Boston Scientific Corporation, Bristol-Myers Squibb Company, Cisco Systems, Inc., Fate Therapeutics, GE Healthcare Life Sciences, Generex Biotechnology Corporation, Idera Pharmaceuticals, Inc., Nante Health, Neurometrics, Inc., NuGenerex, Repligen Corporation, Sesen Bio, Inc., T2 Biosystems, and Vericel Corporation.
Other authors have no declarations of interest.

References

Agrawal, S., and Fox, J.H. (2019). Novel proteomic changes in brain mitochondria provide insights into mitochondrial dysfunction in mouse models of Huntington's disease. *Mitochondrion* 47**,** 318-329.

Alterman, J.F., Godinho, B., Hassler, M.R., Ferguson, C.M., Echeverria, D., Sapp, E., Haraszti, R.A., Coles, A.H., Conroy, F., Miller, R., Roux, L., Yan, P., Knox, E.G., Turanov, A.A., King, R.M., Gernoux, G., Mueller, C., Gray-Edwards, H.L., Moser, R.P., Bishop, N.C., Jaber, S.M., Gounis, M.J., Sena-Esteves, M., Pai, A.A., Difiglia, M., Aronin, N., and Khvorova, A. (2019). A divalent siRNA chemical scaffold for potent and sustained modulation of gene expression throughout the central nervous system. *Nat Biotechnol* 37**,** 884-894.

Atwal, R.S., Xia, J., Pinchev, D., Taylor, J., Epand, R.M., and Truant, R. (2007). Huntingtin has a membrane association signal that can modulate huntingtin aggregation, nuclear entry and toxicity. *Hum Mol Genet* 16**,** 2600-2615.

Barron, J.C., Hurley, E.P., and Parsons, M.P. (2021). Huntingtin and the Synapse. *Front Cell Neurosci* 15**,** 689332.

Benraiss, A., Mariani, J.N., Tate, A., Madsen, P.M., Clark, K.M., Welle, K.A., Solly, R., Capellano, L., Bentley, K., Chandler-Militello, D., and Goldman, S.A. (2022). A TCF7L2-responsive suppression of both homeostatic and compensatory remyelination in Huntington disease mice. *Cell Rep* 40**,** 111291.

Berridge, M.J. (2016). The Inositol Trisphosphate/Calcium Signaling Pathway in Health and Disease. *Physiol Rev* 96**,** 1261-1296.

Bertoglio, D., Bard, J., Hessmann, M., Liu, L., Gartner, A., De Lombaerde, S., Huscher, B., Zajicek, F., Miranda, A., Peters, F., Herrmann, F., Schaertl, S., Vasilkovska, T., Brown, C.J., Johnson, P.D., Prime, M.E., Mills, M.R., Van Der Linden, A., Mrzljak, L., Khetarpal, V., Wang, Y., Marchionini, D.M., Skinbjerg, M., Verhaeghe, J., Dominguez, C., Staelens, S., and Munoz-Sanjuan, I. (2022). Development of a ligand for in vivo imaging of mutant huntingtin in Huntington's disease. *Sci Transl Med* 14**,** eabm3682.

Bibb, J.A., Yan, Z., Svenningsson, P., Snyder, G.L., Pieribone, V.A., Horiuchi, A., Nairn, A.C., Messer, A., and Greengard, P. (2000). Severe deficiencies in dopamine signaling in presymptomatic Huntington's disease mice. *Proc Natl Acad Sci U S A* 97**,** 6809-6814.

Blunsom, N.J., and Cockcroft, S. (2020). CDP-Diacylglycerol Synthases (CDS): Gateway to Phosphatidylinositol and Cardiolipin Synthesis. *Front Cell Dev Biol* 8**,** 63.

Bosio, A., Binczek, E., and Stoffel, W. (1996). Functional breakdown of the lipid bilayer of the myelin membrane in central and peripheral nervous system by disrupted galactocerebroside synthesis. *Proc Natl Acad Sci U S A* 93**,** 13280-13285.

Boudreau, R.L., Mcbride, J.L., Martins, I., Shen, S., Xing, Y., Carter, B.J., and Davidson, B.L. (2009). Nonallele-specific silencing of mutant and wild-type huntingtin demonstrates therapeutic efficacy in Huntington's disease mice. *Mol Ther* 17**,** 1053-1063.

Bourbon-Teles, J., Bells, S., Jones, D.K., Coulthard, E., Rosser, A., and Metzler-Baddeley, C. (2019). Myelin Breakdown in Human Huntington's Disease: Multi-Modal Evidence from Diffusion MRI and Quantitative Magnetization Transfer. *Neuroscience* 403**,** 79-92.

Breitkopf, S.B., Ricoult, S.J.H., Yuan, M., Xu, Y., Peake, D.A., Manning, B.D., and Asara, J.M. (2017). A relative quantitative positive/negative ion switching method for untargeted lipidomics via high resolution LC-MS/MS from any biological source. *Metabolomics* 13.

Caron, N.S., Banos, R., Aly, A.E., Xie, Y., Ko, S., Potluri, N., Anderson, C., Black, H.F., Anderson, L.M., Gordon, B., Southwell, A.L., and Hayden, M.R. (2022). Cerebrospinal fluid mutant huntingtin is a biomarker for huntingtin lowering in the striatum of Huntington disease mice. *Neurobiol Dis* 166**,** 105652.

Caron, N.S., Banos, R., Yanick, C., Aly, A.E., Byrne, L.M., Smith, E.D., Xie, Y., Smith, S.E.P., Potluri, N., Findlay Black, H., Casal, L., Ko, S., Cheung, D., Kim, H., Seong, I.S., Wild, E.J., Song, J.J., Hayden, M.R., and Southwell, A.L. (2021). Mutant Huntingtin Is Cleared from the Brain via Active Mechanisms in Huntington Disease. *J Neurosci* 41**,** 780-796.

Carroll, J.B., Deik, A., Fossale, E., Weston, R.M., Guide, J.R., Arjomand, J., Kwak, S., Clish, C.B., and Macdonald, M.E. (2015). HdhQ111 Mice Exhibit Tissue Specific Metabolite Profiles that Include Striatal Lipid Accumulation. *PLoS One* 10**,** e0134465.

Caviston, J.P., and Holzbaur, E.L. (2009). Huntingtin as an essential integrator of intracellular vesicular trafficking. *Trends Cell Biol* 19**,** 147-155.

Chaibva, M., Gao, X., Jain, P., Campbell, W.a.T., Frey, S.L., and Legleiter, J. (2018). Sphingomyelin and GM1 Influence Huntingtin Binding to, Disruption of, and Aggregation on Lipid Membranes. *ACS Omega* 3**,** 273-285.

Coetzee, T., Fujita, N., Dupree, J., Shi, R., Blight, A., Suzuki, K., Suzuki, K., and Popko, B. (1996). Myelination in the absence of galactocerebroside and sulfatide: normal structure with abnormal function and regional instability. *Cell* 86**,** 209-219.

Coffey, S.R., Andrew, M., Ging, H., Hamilton, J., Flower, M., Kovalenko, M., Bragg, R.M., Cantle, J.P., Mchugh, C.A., Carrillo, J.M., Rodier, J., Marchionini, D.M., Wilkinson, H.A., Kwak, S., Howland, D.S., Bennett, C.F., Mouro Pinto, R., Auburger, G., Zeitlin, S.O., Kordasiewicz, H.B., Tabrizi, S.J., Wheeler, V.C., and Carroll, J.B. (2020). *Huntintin lowering reduces somatic instability at CAG-expanded loci* [Online]. bioRxiv. Available: bioRxiv 2020.07.23.218347; doi: https://doi.org/10.1101/2020.07.23.218347 [Accessed].

Cronin, C.A., Gluba, W., and Scrable, H. (2001). The lac operator-repressor system is functional in the mouse. *Genes Dev* 15**,** 1506-1517.

Dai, J., Bercury, K.K., Ahrendsen, J.T., and Macklin, W.B. (2015). Olig1 function is required for oligodendrocyte differentiation in the mouse brain. *J Neurosci* 35**,** 4386-4402.

Datson, N.A., Gonzalez-Barriga, A., Kourkouta, E., Weij, R., Van De Giessen, J., Mulders, S., Kontkanen, O., Heikkinen, T., Lehtimaki, K., and Van Deutekom, J.C. (2017). The expanded CAG repeat in the huntingtin gene as target for therapeutic RNA modulation throughout the HD mouse brain. *PLoS One* 12**,** e0171127.

De La Monte, S.M., Vonsattel, J.P., and Richardson, E.P., Jr. (1988). Morphometric demonstration of atrophic changes in the cerebral cortex, white matter, and neostriatum in Huntington's disease. *J Neuropathol Exp Neurol* 47**,** 516-525.

Desplats, P.A., Denny, C.A., Kass, K.E., Gilmartin, T., Head, S.R., Sutcliffe, J.G., Seyfried, T.N., and Thomas, E.A. (2007). Glycolipid and ganglioside metabolism imbalances in Huntington's disease. *Neurobiol Dis* 27**,** 265-277.

Di Paola, M., Luders, E., Cherubini, A., Sanchez-Castaneda, C., Thompson, P.M., Toga, A.W., Caltagirone, C., Orobello, S., Elifani, F., Squitieri, F., and Sabatini, U. (2012). Multimodal MRI analysis of the corpus callosum reveals white matter differences in presymptomatic and early Huntington's disease. *Cereb Cortex* 22**,** 2858-2866.

Di Pardo, A., Basit, A., Armirotti, A., Amico, E., Castaldo, S., Pepe, G., Marracino, F., Buttari, F., Digilio, A.F., and Maglione, V. (2017). De novo Synthesis of Sphingolipids Is Defective in Experimental Models of Huntington's Disease. *Front Neurosci* 11**,** 698.

Diaz-Hernandez, M., Torres-Peraza, J., Salvatori-Abarca, A., Moran, M.A., Gomez-Ramos, P., Alberch, J., and Lucas, J.J. (2005). Full motor recovery despite striatal neuron loss and formation of irreversible amyloid-like inclusions in a conditional mouse model of Huntington's disease. *J Neurosci* 25**,** 9773-9781.

Difiglia, M., Sapp, E., Chase, K., Schwarz, C., Meloni, A., Young, C., Martin, E., Vonsattel, J.P., Carraway, R., Reeves, S.A., and Et Al. (1995). Huntingtin is a cytoplasmic protein associated with vesicles in human and rat brain neurons. *Neuron* 14**,** 1075-1081.

Difiglia, M., Sena-Esteves, M., Chase, K., Sapp, E., Pfister, E., Sass, M., Yoder, J., Reeves, P., Pandey, R.K., Rajeev, K.G., Manoharan, M., Sah, D.W., Zamore, P.D., and Aronin, N. (2007). Therapeutic silencing of mutant huntingtin with siRNA attenuates striatal and cortical neuropathology and behavioral deficits. *Proc Natl Acad Sci U S A* 104**,** 17204-17209.

Dragatsis, I., Levine, M.S., and Zeitlin, S. (2000). Inactivation of Hdh in the brain and testis results in progressive neurodegeneration and sterility in mice. *Nat Genet* 26**,** 300-306.

Drouet, V., Perrin, V., Hassig, R., Dufour, N., Auregan, G., Alves, S., Bonvento, G., Brouillet, E., Luthi-Carter, R., Hantraye, P., and Deglon, N. (2009). Sustained effects of nonallele-specific Huntingtin silencing. *Ann Neurol* 65**,** 276-285.

Duyao, M.P., Auerbach, A.B., Ryan, A., Persichetti, F., Barnes, G.T., Mcneil, S.M., Ge, P., Vonsattel, J.P., Gusella, J.F., Joyner, A.L., and Et Al. (1995). Inactivation of the mouse Huntington's disease gene homolog Hdh. *Science* 269**,** 407-410.

Edvardson, S., Hama, H., Shaag, A., Gomori, J.M., Berger, I., Soffer, D., Korman, S.H., Taustein, I., Saada, A., and Elpeleg, O. (2008). Mutations in the fatty acid 2-hydroxylase gene are associated with leukodystrophy with spastic paraparesis and dystonia. *Am J Hum Genet* 83**,** 643-648.

Faria, A.V., Ratnanather, J.T., Tward, D.J., Lee, D.S., Van Den Noort, F., Wu, D., Brown, T., Johnson, H., Paulsen, J.S., Ross, C.A., Younes, L., Miller, M.I., Investigators, P.-H., and Coordinators of the Huntington Study, G. (2016). Linking white matter and deep gray matter alterations in premanifest Huntington disease. *Neuroimage Clin* 11**,** 450-460.

Ferrari Bardile, C., Garcia-Miralles, M., Caron, N.S., Rayan, N.A., Langley, S.R., Harmston, N., Rondelli, A.M., Teo, R.T.Y., Waltl, S., Anderson, L.M., Bae, H.G., Jung, S., Williams, A., Prabhakar, S., Petretto, E., Hayden, M.R., and Pouladi,

M.A. (2019). Intrinsic mutant HTT-mediated defects in oligodendroglia cause myelination deficits and behavioral abnormalities in Huntington disease. *Proc Natl Acad Sci U S A* 116**,** 9622-9627.

Fitzner, D., Bader, J.M., Penkert, H., Bergner, C.G., Su, M., Weil, M.T., Surma, M.A., Mann, M., Klose, C., and Simons, M. (2020). Cell-Type- and Brain-Region-Resolved Mouse Brain Lipidome. *Cell Rep* 32**,** 108132.

Fox, L.M., Kim, K., Johnson, C.W., Chen, S., Croce, K.R., Victor, M.B., Eenjes, E., Bosco, J.R., Randolph, L.K., Dragatsis, I., Dragich, J.M., Yoo, A.S., and Yamamoto, A. (2020). Huntington's Disease Pathogenesis Is Modified In Vivo by Alfy/Wdfy3 and Selective Macroautophagy. *Neuron* 105**,** 813-821 e816.

Gao, R., Chakraborty, A., Geater, C., Pradhan, S., Gordon, K.L., Snowden, J., Yuan, S., Dickey, A.S., Choudhary, S., Ashizawa, T., Ellerby, L.M., La Spada, A.R., Thompson, L.M., Hazra, T.K., and Sarkar, P.S. (2019). Mutant huntingtin impairs PNKP and ATXN3, disrupting DNA repair and transcription. *Elife* 8.

Goedhart, J., and Luijsterburg, M.S. (2020). VolcaNoseR is a web app for creating, exploring, labeling and sharing volcano plots. *Sci Rep* 10**,** 20560.

Gu, M., Gash, M.T., Mann, V.M., Javoy-Agid, F., Cooper, J.M., and Schapira, A.H. (1996). Mitochondrial defect in Huntington's disease caudate nucleus. *Ann Neurol* 39**,** 385-389.

Hardt, R., Jordans, S., Winter, D., Gieselmann, V., Wang-Eckhardt, L., and Eckhardt, M. (2021). Decreased turnover of the CNS myelin protein Opalin in a mouse model of hereditary spastic paraplegia 35. *Hum Mol Genet* 29**,** 3616-3630.

Hirt, U.A., and Leist, M. (2003). Rapid, noninflammatory and PS-dependent phagocytic clearance of necrotic cells. *Cell Death Differ* 10**,** 1156-1164.

Hobbs, N.Z., Henley, S.M., Ridgway, G.R., Wild, E.J., Barker, R.A., Scahill, R.I., Barnes, J., Fox, N.C., and Tabrizi, S.J. (2010). The progression of regional atrophy in premanifest and early Huntington's disease: a longitudinal voxel-based morphometry study. *J Neurol Neurosurg Psychiatry* 81**,** 756-763.

Inoue, T., Dehmukh, D.S., and Pieringer, R.A. (1971). The association of the galactosyl diglycerides of brain with myelination. I. Changes in the concentration of monogalactosyl diglyceride in the somal and myelin fractions of brain of rats during development. *J Biol Chem* 246**,** 5688-5694.

Iuliano, M., Seeley, C., Sapp, E., Jones, E.L., Martin, C., Li, X., Difiglia, M., and Kegel-Gleason, K.B. (2021). Disposition of Proteins and Lipids in Synaptic Membrane Compartments Is Altered in Q175/Q7 Huntington's Disease Mouse Striatum. *Front Synaptic Neurosci* 13**,** 618391.

Jin, J., Peng, Q., Hou, Z., Jiang, M., Wang, X., Langseth, A.J., Tao, M., Barker, P.B., Mori, S., Bergles, D.E., Ross, C.A., Detloff, P.J., Zhang, J., and Duan, W. (2015). Early white matter abnormalities, progressive brain pathology and motor deficits in a novel knock-in mouse model of Huntington's disease. *Hum Mol Genet* 24**,** 2508-2527.

Kaganovich, D., Kopito, R., and Frydman, J. (2008). Misfolded proteins partition between two distinct quality control compartments. *Nature* 454**,** 1088-1095.

Keeler, A.M., Sapp, E., Chase, K., Sottosanti, E., Danielson, E., Pfister, E., Stoica, L., Difiglia, M., Aronin, N., and Sena-Esteves, M. (2016). Cellular Analysis of Silencing the Huntington's Disease Gene Using AAV9 Mediated Delivery of Artificial Micro RNA into the Striatum of Q140/Q140 Mice. *J Huntingtons Dis* 5**,** 239-248.

Kegel-Gleason, K.B. (2013). Huntingtin interactions with membrane phospholipids: strategic targets for therapeutic intervention? *J Huntingtons Dis* 2**,** 239-250.

Kegel, K.B., Kim, M., Sapp, E., Mcintyre, C., Castano, J.G., Aronin, N., and Difiglia, M. (2000). Huntingtin expression stimulates endosomal-lysosomal activity, endosome tubulation, and autophagy. *J Neurosci* 20**,** 7268-7278.

Kegel, K.B., Sapp, E., Alexander, J., Valencia, A., Reeves, P., Li, X., Masso, N., Sobin, L., Aronin, N., and Difiglia, M. (2009a). Polyglutamine expansion in huntingtin alters its interaction with phospholipids. *J Neurochem* 110**,** 1585-1597.

Kegel, K.B., Schewkunow, V., Sapp, E., Masso, N., Wanker, E.E., Difiglia, M., and Goldmann, W.H. (2009b). Polyglutamine expansion in huntingtin increases its insertion into lipid bilayers. *Biochem Biophys Res Commun* 387**,** 472-475.

Keller, C.G., Shin, Y., Monteys, A.M., Renaud, N., Beibel, M., Teider, N., Peters, T., Faller, T., St-Cyr, S., Knehr, J., Roma, G., Reyes, A., Hild, M., Lukashev, D., Theil, D., Dales, N., Cha, J.H., Borowsky, B., Dolmetsch, R., Davidson, B.L., and Sivasankaran, R. (2022). An orally available, brain penetrant, small molecule lowers huntingtin levels by enhancing pseudoexon inclusion. *Nat Commun* 13**,** 1150.

Kim, H.Y., Huang, B.X., and Spector, A.A. (2014). Phosphatidylserine in the brain: metabolism and function. *Prog Lipid Res* 56**,** 1-18.

Ko, J., Isas, J.M., Sabbaugh, A., Yoo, J.H., Pandey, N.K., Chongtham, A., Ladinsky, M., Wu, W.L., Rohweder, H., Weiss, A., Macdonald, D., Munoz-Sanjuan, I., Langen, R., Patterson, P.H., and Khoshnan, A. (2018). Identification of distinct

conformations associated with monomers and fibril assemblies of mutant huntingtin. *Hum Mol Genet* 27**,** 2330-2343.

Koelmel, J.P., Ulmer, C.Z., Jones, C.M., Yost, R.A., and Bowden, J.A. (2017). Common cases of improper lipid annotation using high-resolution tandem mass spectrometry data and corresponding limitations in biological interpretation. *Biochim Biophys Acta Mol Cell Biol Lipids* 1862**,** 766-770.

Kordasiewicz, H.B., Stanek, L.M., Wancewicz, E.V., Mazur, C., Mcalonis, M.M., Pytel, K.A., Artates, J.W., Weiss, A., Cheng, S.H., Shihabuddin, L.S., Hung, G., Bennett, C.F., and Cleveland, D.W. (2012). Sustained therapeutic reversal of Huntington's disease by transient repression of huntingtin synthesis. *Neuron* 74**,** 1031-1044.

Landles, C., Sathasivam, K., Weiss, A., Woodman, B., Moffitt, H., Finkbeiner, S., Sun, B., Gafni, J., Ellerby, L.M., Trottier, Y., Richards, W.G., Osmand, A., Paganetti, P., and Bates, G.P. (2010). Proteolysis of mutant huntingtin produces an exon 1 fragment that accumulates as an aggregated protein in neuronal nuclei in Huntington disease. *J Biol Chem* 285**,** 8808-8823.

Langfelder, P., Cantle, J.P., Chatzopoulou, D., Wang, N., Gao, F., Al-Ramahi, I., Lu, X.H., Ramos, E.M., El-Zein, K., Zhao, Y., Deverasetty, S., Tebbe, A., Schaab, C., Lavery, D.J., Howland, D., Kwak, S., Botas, J., Aaronson, J.S., Rosinski, J., Coppola, G., Horvath, S., and Yang, X.W. (2016). Integrated genomics and proteomics define huntingtin CAG length-dependent networks in mice. *Nat Neurosci* 19**,** 623-633.

Leavitt, B.R., Kordasiewicz, H.B., and Schobel, S.A. (2020). Huntingtin-Lowering Therapies for Huntington Disease: A Review of the Evidence of Potential Benefits and Risks. *JAMA Neurol* 77**,** 764-772.

Lim, R.G., Al-Dalahmah, O., Wu, J., Gold, M.P., Reidling, J.C., Tang, G., Adam, M., Dansu, D.K., Park, H.J., Casaccia, P., Miramontes, R., Reyes-Ortiz, A.M., Lau, A., Hickman, R.A., Khan, F., Paryani, F., Tang, A., Ofori, K., Miyoshi, E., Michael, N., Mcclure, N., Flowers, X.E., Vonsattel, J.P., Davidson, S., Menon, V., Swarup, V., Fraenkel, E., Goldman, J.E., and Thompson, L.M. (2022). Huntington disease oligodendrocyte maturation deficits revealed by single-nucleus RNAseq are rescued by thiamine-biotin supplementation. *Nat Commun* 13**,** 7791.

Marchionini, D.M., Liu, J.P., Ambesi-Impiombato, A., Kerker, K., Cirillo, K., Bansal, M., Mushlin, R., Brunner, D., Ramboz, S., Kwan, M., Kuhlbrodt, K., Tillack, K., Peters, F., Rauhala, L., Obenauer, J., Greene, J.R., Hartl, C., Khetarpal, V., Lager, B., Rosinski, J., Aaronson, J., Alam, M., Signer, E., Munoz-Sanjuan, I., Howland, D., and Zeitlin, S.O. (2022). Benefits of global mutant huntingtin lowering diminish over time in a Huntington's disease mouse model. *JCI Insight* 7.

Matsui, J.T., Vaidya, J.G., Wassermann, D., Kim, R.E., Magnotta, V.A., Johnson, H.J., Paulsen, J.S., Investigators, P.-H., and Coordinators of the Huntington Study, G. (2015). Prefrontal cortex white matter tracts in prodromal Huntington disease. *Hum Brain Mapp* 36**,** 3717-3732.

Matyash, V., Liebisch, G., Kurzchalia, T.V., Shevchenko, A., and Schwudke, D. (2008). Lipid extraction by methyl-tert-butyl ether for high-throughput lipidomics. *J Lipid Res* 49**,** 1137-1146.

Mcbride, J.L., Pitzer, M.R., Boudreau, R.L., Dufour, B., Hobbs, T., Ojeda, S.R., and Davidson, B.L. (2011). Preclinical safety of RNAi-mediated HTT suppression in the rhesus macaque as a potential therapy for Huntington's disease. *Mol Ther* 19**,** 2152-2162.

Mckinstry, S.U., Karadeniz, Y.B., Worthington, A.K., Hayrapetyan, V.Y., Ozlu, M.I., Serafin-Molina, K., Risher, W.C., Ustunkaya, T., Dragatsis, I., Zeitlin, S., Yin, H.H., and Eroglu, C. (2014). Huntingtin is required for normal excitatory synapse development in cortical and striatal circuits. *J Neurosci* 34**,** 9455-9472.

Mcquade, L.R., Balachandran, A., Scott, H.A., Khaira, S., Baker, M.S., and Schmidt, U. (2014). Proteomics of Huntington's disease-affected human embryonic stem cells reveals an evolving pathology involving mitochondrial dysfunction and metabolic disturbances. *J Proteome Res* 13**,** 5648-5659.

Mehler, M.F., Petronglo, J.R., Arteaga-Bracho, E.E., Gulinello, M.E., Winchester, M.L., Pichamoorthy, N., Young, S.K., Dejesus, C.D., Ishtiaq, H., Gokhan, S., and Molero, A.E. (2019). Loss-of-Huntingtin in Medial and Lateral Ganglionic Lineages Differentially Disrupts Regional Interneuron and Projection Neuron Subtypes and Promotes Huntington's Disease-Associated Behavioral, Cellular, and Pathological Hallmarks. *J Neurosci* 39**,** 1892-1909.

Mehta, S.R., Tom, C.M., Wang, Y., Bresee, C., Rushton, D., Mathkar, P.P., Tang, J., and Mattis, V.B. (2018). Human Huntington's Disease iPSC-Derived Cortical Neurons Display Altered Transcriptomics, Morphology, and Maturation. *Cell Rep* 25**,** 1081-1096 e1086.

Menalled, L.B., Sison, J.D., Dragatsis, I., Zeitlin, S., and Chesselet, M.F. (2003). Time course of early motor and neuropathological anomalies in a knock-in mouse model of Huntington's disease with 140 CAG repeats. *J Comp Neurol* 465**,** 11-26.

Nasir, J., Floresco, S.B., O'kusky, J.R., Diewert, V.M., Richman, J.M., Zeisler, J., Borowski, A., Marth, J.D., Phillips, A.G., and Hayden, M.R. (1995). Targeted disruption of the Huntington's disease gene results in embryonic lethality and behavioral and morphological changes in heterozygotes. *Cell* 81**,** 811-823.

Nopoulos, P.C. (2016). Huntington disease: a single-gene degenerative disorder of the striatum. *Dialogues Clin Neurosci* 18**,** 91-98.

O'brien, J.S., and Sampson, E.L. (1965). Lipid composition of the normal human brain: gray matter, white matter, and myelin. *J Lipid Res* 6**,** 537-544.

O'kusky, J.R., Nasir, J., Cicchetti, F., Parent, A., and Hayden, M.R. (1999). Neuronal degeneration in the basal ganglia and loss of pallido-subthalamic synapses in mice with targeted disruption of the Huntington's disease gene. *Brain Res* 818**,** 468-479.

Odish, O.F., Leemans, A., Reijntjes, R.H., Van Den Bogaard, S.J., Dumas, E.M., Wolterbeek, R., Tax, C.M., Kuijf, H.J., Vincken, K.L., Van Der Grond, J., and Roos, R.A. (2015). Microstructural brain abnormalities in Huntington's disease: A two-year follow-up. *Hum Brain Mapp* 36**,** 2061-2074.

Oh, S.L., Chen, C.M., Wu, Y.R., Valdes Hernandez, M., Tsai, C.C., Cheng, J.S., Chen, Y.L., Wu, Y.M., Lin, Y.C., and Wang, J.J. (2021). Fixel-Based Analysis Effectively Identifies White Matter Tract Degeneration in Huntington's Disease. *Front Neurosci* 15**,** 711651.

Osipovitch, M., Asenjo Martinez, A., Mariani, J.N., Cornwell, A., Dhaliwal, S., Zou, L., Chandler-Militello, D., Wang, S., Li, X., Benraiss, S.J., Agate, R., Lampp, A., Benraiss, A., Windrem, M.S., and Goldman, S.A. (2019). Human ESC-Derived Chimeric Mouse Models of Huntington's Disease Reveal Cell-Intrinsic Defects in Glial Progenitor Cell Differentiation. *Cell Stem Cell* 24**,** 107-122 e107.

Oyama, F., Miyazaki, H., Sakamoto, N., Becquet, C., Machida, Y., Kaneko, K., Uchikawa, C., Suzuki, T., Kurosawa, M., Ikeda, T., Tamaoka, A., Sakurai, T., and Nukina, N. (2006). Sodium channel beta4 subunit: down-regulation and possible involvement in neuritic degeneration in Huntington's disease transgenic mice. *J Neurochem* 98**,** 518-529.

Paulsen, J.S. (2009). Functional imaging in Huntington's disease. *Exp Neurol* 216**,** 272-277.

Paulsen, J.S., Langbehn, D.R., Stout, J.C., Aylward, E., Ross, C.A., Nance, M., Guttman, M., Johnson, S., Macdonald, M., Beglinger, L.J., Duff, K., Kayson, E., Biglan, K., Shoulson, I., Oakes, D., Hayden, M., Predict, H.D.I., and Coordinators of the Huntington Study, G. (2008). Detection of Huntington's disease decades before diagnosis: the Predict-HD study. *J Neurol Neurosurg Psychiatry* 79**,** 874-880.

Perot, J.B., Celestine, M., Palombo, M., Dhenain, M., Humbert, S., Brouillet, E., and Flament, J. (2022). Longitudinal multimodal MRI characterization of a knock-in mouse model of Huntington's disease reveals early gray and white matter alterations. *Hum Mol Genet* 31**,** 3581-3596.

Petersen, A., and Bjorkqvist, M. (2006). Hypothalamic-endocrine aspects in Huntington's disease. *Eur J Neurosci* 24**,** 961-967.

Phillips, G.R., Saville, J.T., Hancock, S.E., Brown, S.H.J., Jenner, A.M., Mclean, C., Fuller, M., Newell, K.A., and Mitchell, T.W. (2022). The long and the short of Huntington's disease: how the sphingolipid profile is shifted in the caudate of advanced clinical cases. *Brain Commun* 4**,** fcab303.

Phillips, O., Sanchez-Castaneda, C., Elifani, F., Maglione, V., Di Pardo, A., Caltagirone, C., Squitieri, F., Sabatini, U., and Di Paola, M. (2013). Tractography of the corpus callosum in Huntington's disease. *PLoS One* 8**,** e73280.

Phillips, O., Squitieri, F., Sanchez-Castaneda, C., Elifani, F., Caltagirone, C., Sabatini, U., and Di Paola, M. (2014). Deep white matter in Huntington's disease. *PLoS One* 9**,** e109676.

Polyansky, A., Shatz, O., Fraiberg, M., Shimoni, E., Dadosh, T., Mari, M., Reggiori, F.M., Qin, C., Han, X., and Elazar, Z. (2022). Phospholipid imbalance impairs autophagosome completion. *EMBO J* 41**,** e110771.

Poudel, G.R., Stout, J.C., Dominguez, D.J., Churchyard, A., Chua, P., Egan, G.F., and Georgiou-Karistianis, N. (2015). Longitudinal change in white matter microstructure in Huntington's disease: The IMAGE-HD study. *Neurobiol Dis* 74**,** 406-412.

Qin, Z.H., Wang, Y., Kegel, K.B., Kazantsev, A., Apostol, B.L., Thompson, L.M., Yoder, J., Aronin, N., and Difiglia, M. (2003). Autophagy regulates the processing of amino terminal huntingtin fragments. *Hum Mol Genet* 12**,** 3231-3244.

Rattray, I., Smith, E.J., Crum, W.R., Walker, T.A., Gale, R., Bates, G.P., and Modo, M. (2013). Correlations of behavioral deficits with brain pathology assessed through longitudinal MRI and histopathology in the R6/1 mouse model of Huntington's disease. *PLoS One* 8**,** e84726.

Reza, S., Ugorski, M., and Suchanski, J. (2021). Glucosylceramide and galactosylceramide, small glycosphingolipids with significant impact on health and disease. *Glycobiology* 31**,** 1416-1434.

Rodriguez-Lebron, E., Denovan-Wright, E.M., Nash, K., Lewin, A.S., and Mandel, R.J. (2005). Intrastriatal rAAV-mediated delivery of anti-huntingtin shRNAs induces partial reversal of disease progression in R6/1 Huntington's disease transgenic mice. *Mol Ther* 12**,** 618-633.

Rosas, H.D., Tuch, D.S., Hevelone, N.D., Zaleta, A.K., Vangel, M., Hersch, S.M., and Salat, D.H. (2006). Diffusion tensor imaging in presymptomatic and early Huntington's disease: Selective white matter pathology and its relationship to clinical measures. *Mov Disord* 21**,** 1317-1325.

Sapp, E., Kegel, K.B., Aronin, N., Hashikawa, T., Uchiyama, Y., Tohyama, K., Bhide, P.G., Vonsattel, J.P., and Difiglia, M. (2001). Early and progressive accumulation of reactive microglia in the Huntington disease brain. *J Neuropathol Exp Neurol* 60**,** 161-172.

Sapp, E., Seeley, C., Iuliano, M., Weisman, E., Vodicka, P., Difiglia, M., and Kegel-Gleason, K.B. (2020). Protein changes in synaptosomes of Huntington's disease knock-in mice are dependent on age and brain region. *Neurobiol Dis* 141**,** 104950.

Saudou, F., and Humbert, S. (2016). The Biology of Huntingtin. *Neuron* 89**,** 910-926.

Savage, J.C., St-Pierre, M.K., Carrier, M., El Hajj, H., Novak, S.W., Sanchez, M.G., Cicchetti, F., and Tremblay, M.E. (2020). Microglial physiological properties and interactions with synapses are altered at presymptomatic stages in a mouse model of Huntington's disease pathology. *J Neuroinflammation* 17**,** 98.

Scherzinger, E., Lurz, R., Turmaine, M., Mangiarini, L., Hollenbach, B., Hasenbank, R., Bates, G.P., Davies, S.W., Lehrach, H., and Wanker, E.E. (1997). Huntingtin-encoded polyglutamine expansions form amyloid-like protein aggregates in vitro and in vivo. *Cell* 90**,** 549-558.

Schmidt-Schultz, T., and Althaus, H.H. (1994). Monogalactosyl diglyceride, a marker for myelination, activates oligodendroglial protein kinase C. *J Neurochem* 62**,** 1578-1585.

Scott-Hewitt, N., Perrucci, F., Morini, R., Erreni, M., Mahoney, M., Witkowska, A., Carey, A., Faggiani, E., Schuetz, L.T., Mason, S., Tamborini, M., Bizzotto, M., Passoni, L., Filipello, F., Jahn, R., Stevens, B., and Matteoli, M. (2020). Local externalization of phosphatidylserine mediates developmental synaptic pruning by microglia. *EMBO J* 39**,** e105380.

Scrable, H. (2002). Say when: reversible control of gene expression in the mouse by lac. *Semin Cell Dev Biol* 13**,** 109-119.

Sharp, A.H., Loev, S.J., Schilling, G., Li, S.H., Li, X.J., Bao, J., Wagster, M.V., Kotzuk, J.A., Steiner, J.P., Lo, A., and Et Al. (1995). Widespread expression of Huntington's disease gene (IT15) protein product. *Neuron* 14**,** 1065-1074.

Singh, S., Mehta, H., and Fekete, R. (2013). Altered Fractional Anisotropy in Early Huntington's Disease. *Case Rep Neurol* 5**,** 26-30.

Skene, D.J., Middleton, B., Fraser, C.K., Pennings, J.L., Kuchel, T.R., Rudiger, S.R., Bawden, C.S., and Morton, A.J. (2017). Metabolic profiling of presymptomatic Huntington's disease sheep reveals novel biomarkers. *Sci Rep* 7**,** 43030.

Skotte, N.H., Andersen, J.V., Santos, A., Aldana, B.I., Willert, C.W., Norremolle, A., Waagepetersen, H.S., and Nielsen, M.L. (2018). Integrative Characterization of the R6/2 Mouse Model of Huntington's Disease Reveals Dysfunctional Astrocyte Metabolism. *Cell Rep* 23**,** 2211-2224.

Southwell, A.L., Kordasiewicz, H.B., Langbehn, D., Skotte, N.H., Parsons, M.P., Villanueva, E.B., Caron, N.S., Ostergaard, M.E., Anderson, L.M., Xie, Y., Cengio, L.D., Findlay-Black, H., Doty, C.N., Fitsimmons, B., Swayze, E.E., Seth, P.P., Raymond, L.A., Frank Bennett, C., and Hayden, M.R. (2018). Huntingtin suppression restores cognitive function in a mouse model of Huntington's disease. *Sci Transl Med* 10.

Southwell, A.L., Smith, S.E., Davis, T.R., Caron, N.S., Villanueva, E.B., Xie, Y., Collins, J.A., Ye, M.L., Sturrock, A., Leavitt, B.R., Schrum, A.G., and Hayden, M.R. (2015). Ultrasensitive measurement of huntingtin protein in cerebrospinal fluid demonstrates increase with Huntington disease stage and decrease following brain huntingtin suppression. *Sci Rep* 5**,** 12166.

Stanek, L.M., Sardi, S.P., Mastis, B., Richards, A.R., Treleaven, C.M., Taksir, T., Misra, K., Cheng, S.H., and Shihabuddin, L.S. (2014). Silencing mutant huntingtin by adeno-associated virus-mediated RNA interference ameliorates disease manifestations in the YAC128 mouse model of Huntington's disease. *Hum Gene Ther* 25**,** 461-474.

Stanek, L.M., Yang, W., Angus, S., Sardi, P.S., Hayden, M.R., Hung, G.H., Bennett, C.F., Cheng, S.H., and Shihabuddin, L.S. (2013). Antisense oligonucleotide-mediated correction of transcriptional dysregulation is correlated with behavioral benefits in the YAC128 mouse model of Huntington's disease. *J Huntingtons Dis* 2**,** 217-228.

Steventon, J.J., Trueman, R.C., Ma, D., Yhnell, E., Bayram-Weston, Z., Modat, M., Cardoso, J., Ourselin, S., Lythgoe, M., Stewart, A., Rosser, A.E., and Jones, D.K. (2016). Longitudinal in vivo MRI in a Huntington's disease mouse model: Global atrophy in the absence of white matter microstructural damage. *Sci Rep* 6**,** 32423.

Sweidan, W., Bao, F., Bozorgzad, N.S., and George, E. (2020). White and Gray Matter Abnormalities in Manifest Huntington's Disease: Cross-Sectional and Longitudinal Analysis. *J Neuroimaging* 30**,** 351-358.

Tabrizi, S.J., Ghosh, R., and Leavitt, B.R. (2019). Huntingtin Lowering Strategies for Disease Modification in Huntington's Disease. *Neuron* 101**,** 801-819.

Taghian, T., Gallagher, J., Batcho, E., Pullan, C., Kuchel, T., Denney, T., Perumal, R., Moore, S., Muirhead, R., Herde, P., Johns, D., Christou, C., Taylor, A., Passler, T., Pulaparthi, S., Hall, E., Chandra, S., O'neill, C.A., and Gray-Edwards, H. (2022). Brain Alterations in Aged OVT73 Sheep Model of Huntington's Disease: An MRI Based Approach. *J Huntingtons Dis*.

Teo, R.T., Hong, X., Yu-Taeger, L., Huang, Y., Tan, L.J., Xie, Y., To, X.V., Guo, L., Rajendran, R., Novati, A., Calaminus, C., Riess, O., Hayden, M.R., Nguyen, H.P., Chuang, K.H., and Pouladi, M.A. (2016). Structural and molecular myelination deficits occur prior to neuronal loss in the YAC128 and BACHD models of Huntington disease. *Hum Mol Genet* 25**,** 2621-2632.

Teo, R.T.Y., Ferrari Bardile, C., Tay, Y.L., Yusof, N., Kreidy, C.A., Tan, L.J., and Pouladi, M.A. (2019). Impaired Remyelination in a Mouse Model of Huntington Disease. *Mol Neurobiol* 56**,** 6873-6882.

Tereshchenko, A., Magnotta, V., Epping, E., Mathews, K., Espe-Pfeifer, P., Martin, E., Dawson, J., Duan, W., and Nopoulos, P. (2019). Brain structure in juvenile-onset Huntington disease. *Neurology* 92**,** e1939-e1947.

Velier, J., Kim, M., Schwarz, C., Kim, T.W., Sapp, E., Chase, K., Aronin, N., and Difiglia, M. (1998). Wild-type and mutant huntingtins function in vesicle trafficking in the secretory and endocytic pathways. *Exp Neurol* 152**,** 34-40.

Vodicka, P., Lim, J., Williams, D.T., Kegel, K.B., Chase, K., Park, H., Marchionini, D., Wilkinson, S., Mead, T., Birch, H., Yates, D., Lyons, K., Dominguez, C., Beconi, M., Yue, Z., Aronin, N., and Difiglia, M. (2014). Assessment of chloroquine treatment for modulating autophagy flux in brain of WT and HD mice. *J Huntingtons Dis* 3**,** 159-174.

Vodicka, P., Mo, S., Tousley, A., Green, K.M., Sapp, E., Iuliano, M., Sadri-Vakili, G., Shaffer, S.A., Aronin, N., Difiglia, M., and Kegel-Gleason, K.B. (2015). Mass Spectrometry Analysis of Wild-Type and Knock-in Q140/Q140 Huntington's Disease Mouse Brains Reveals Changes in Glycerophospholipids Including Alterations in Phosphatidic Acid and Lyso-Phosphatidic Acid. *J Huntingtons Dis* 4**,** 187-201.

Vonsattel, J.P., and Difiglia, M. (1998). Huntington disease. *J Neuropathol Exp Neurol* 57**,** 369-384.

Wanker, E.E., Ast, A., Schindler, F., Trepte, P., and Schnoegl, S. (2019). The pathobiology of perturbed mutant huntingtin protein-protein interactions in Huntington's disease. *J Neurochem* 151**,** 507-519.

Weiss, A., Klein, C., Woodman, B., Sathasivam, K., Bibel, M., Regulier, E., Bates, G.P., and Paganetti, P. (2008). Sensitive biochemical aggregate detection reveals aggregation onset before symptom development in cellular and murine models of Huntington's disease. *J Neurochem* 104**,** 846-858.

Williamson, P., and Schlegel, R.A. (2002). Transbilayer phospholipid movement and the clearance of apoptotic cells. *Biochim Biophys Acta* 1585**,** 53-63.

Wilton, D.K., Mastro, K., Heller, M.D., Gergits, F.W., Willing, C.R., Frouin, A., Daggett, A., Gu, X., Kim, A.Y., Faull, R., Jayadev, S., Yednock, T., Yang, X.W., and Stevens, B. (2021). *Microglia mediate early corticostriatal synapse loss and cognitive dysfunction in Huntington's Disease trhough complement-dependent mechanisms* [Online]. bioRxiv. Available: https://doi.org/10.1101/2021.12.03.471180 [Accessed].

Yamamoto, A., Cremona, M.L., and Rothman, J.E. (2006). Autophagy-mediated clearance of huntingtin aggregates triggered by the insulin-signaling pathway. *J Cell Biol* 172**,** 719-731.

Zeitler, B., Froelich, S., Marlen, K., Shivak, D.A., Yu, Q., Li, D., Pearl, J.R., Miller, J.C., Zhang, L., Paschon, D.E., Hinkley, S.J., Ankoudinova, I., Lam, S., Guschin, D., Kopan, L., Cherone, J.M., Nguyen, H.B., Qiao, G., Ataei, Y., Mendel, M.C., Amora, R., Surosky, R., Laganiere, J., Vu, B.J., Narayanan, A., Sedaghat, Y., Tillack, K., Thiede, C., Gartner, A., Kwak, S., Bard, J., Mrzljak, L., Park, L., Heikkinen, T., Lehtimaki, K.K., Svedberg, M.M., Haggkvist, J., Tari, L., Toth, M., Varrone, A., Halldin, C., Kudwa, A.E., Ramboz, S., Day, M., Kondapalli, J., Surmeier, D.J., Urnov, F.D., Gregory, P.D., Rebar, E.J., Munoz-Sanjuan, I., and Zhang, H.S. (2019). Allele-selective transcriptional repression of mutant HTT for the treatment of Huntington's disease. *Nat Med* 25**,** 1131-1142.

Zeitlin, S., Liu, J.P., Chapman, D.L., Papaioannou, V.E., and Efstratiadis, A. (1995). Increased apoptosis and early embryonic lethality in mice nullizygous for the Huntington's disease gene homologue. *Nat Genet* 11**,** 155-163.

Zoller, I., Meixner, M., Hartmann, D., Bussow, H., Meyer, R., Gieselmann, V., and Eckhardt, M. (2008). Absence of 2-hydroxylated sphingolipids is compatible with normal neural development but causes late-onset axon and myelin sheath degeneration. *J Neurosci* 28**,** 9741-9754.

Table 1. 6-month-old LacQ140 mice surveyed by lipidomics

Category	Subclass	% Total Lipid	Species detected	ANOVA p-value	Adjusted p-value (q) n = 36
Glycerophospholipids	PC	42.971	134	0.7415	1
	PE	12.900	152	0.1975	1
	PS	3.810	62	0.1171	1
	PI	1.150	19	0.0189	0.7144
	MePC	0.462	17	0.9859	1
	PA	0.258	13	0.9596	1
	BisMePA	0.245	4	0.1589	1
	dMePE	0.185	9	0.195	1
	PG	0.088	19	0.6255	1
	BisMePE	0.087	1	0.8072	1
	CL	0.069	22	0.5812	1
	PEt	0.065	7	0.3261	1
	PMe	0.009	2	0.8695	1
	PIP2	0.005	2	0.1393	1
	PIP	0.001	1	0.7034	1
	LPC	6.575	30	0.7943	1
	LPE	2.325	23	0.9947	1
	LPS	0.654	7	0.9061	1
	LPI	0.162	7	0.7746	1
	LPG	0.008	4	0.8888	1
	LdMePE	0.004	1	0.4552	1
Glycerolipids	TG	17.706	107	0.5998	1
	MGDG	0.428	3	0.8693	1
	MGMG	0.315	6	0.7537	1
	DG	0.074	13	0.1381	1
	SQMG	0.056	2	0.5986	1
	SQDG	0.001	1	0.9316	1
Sphingolipids	CerG1	4.327	50	0.5466	1
	SM	3.389	47	0.6398	1
	Cer	0.707	14	0.9804	1
	ST	0.404	10	0.3977	1
	So	0.348	3	0.4465	1
	phSM	0.018	4	0.3619	1
	CerG2GNAc1	0.003	1	0.5784	1
Sterol Lipids	ChE	0.011	1	0.5341	1
Fatty Acyls	FA	0.183	2	0.5893	1
TOTAL	**36**		**800**		

Table 1. 6-month-old LacQ140 mice surveyed by lipidomics. Table shows lipids detected in 6-month-old mice, organized by LIPID MAPS category, then by subclass for each respective category. For each subclass the mean detected lipid intensity across all samples was calculated to indicate overall relative abundance *(% Total Lipid*). The number of individual species detected per subclass is listed under *Species Detected. ANOVA P-value* lists p values calculated from one-way analysis of variance (ANOVA) conducted for each subclass; 1 subclass (PI) is statistically significantly different ($p < 0.05$; ANOVA). However, PI did not meet the threshold for significance when correcting for multiple testing. The two-stage linear step-up procedure of Benjamini, Krieger and Yekutieli was used to control the false discovery rate (FDR) over multiple testing (n = 36) with statistical significance accepted at $q < 0.05$. Post-hoc testing revealed that the significant difference was between WT and LacQ140 animals, highlighted in green (Tukey's HSD, multiplicity adjusted $p < 0.05$).

Table 2. 9-month-old LacQ140 mice surveyed by lipidomics

Category	Subclass	% Total Lipid	Species detected	ANOVA p-value	Adjusted p-value (q) n = 24
Glycerophospholipids	PC	44.795	107	0.2928	0.3267
	PE	24.681	154	0.0284	0.0563
	PS	6.760	58	0.0014	0.0125*
	PI	1.113	17	0.0054	0.0168*
	PA	0.232	6	0.7008	0.5957
	BisMePA	0.214	1	0.0041	0.0168*
	MePC	0.136	7	0.4901	0.486
	PG	0.038	4	0.4685	0.486
	dMePE	0.024	2	0.2041	0.269
	PEt	0.014	2	0.9792	0.7283
	BiotinylPE	0.011	1	0.8078	0.6554
	LPC	1.151	10	0.6835	0.5957
	LPE	0.772	16	0.6396	0.5957
	LPS	0.103	5	0.211	0.269
	LPI	0.004	1	0.1715	0.2551
Glycerolipids	TG	3.433	44	0.0057	0.0168
	DG	2.069	70	0.1174	0.1905
	MGDG	0.005	2	0.0005	0.0089*
Sphingolipids	Hex1Cer	9.767	85	0.0243	0.0542
	SM	3.499	23	0.0066	0.0168*
	ST	0.577	9	0.2283	0.2717
	Cer	0.323	6	0.0048	0.0168
	CerPE	0.120	1	0.0766	0.1367
Sterol lipids	ChE	0.160	1	0.918	0.7124
TOTAL	**24**		**632**		

Table 2. 9-month-old LacQ140 mice surveyed by lipidomics. Table shows lipids detected in 9-month-old mice, organized by LIPID MAPS category, then by subclass for each respective category. For each subclass the mean detected lipid intensity across all samples was calculated to indicate overall relative abundance *(% Total Lipid*). The number of individual species detected per subclass is listed under *Species Detected. ANOVA P-value* lists p values calculated from one-way analysis of variance (ANOVA) conducted for each subclass; 9 subclasses (PE, PS, PI, BisMePA, TG, MGDG, Hex1Cer, SM, ST, Cer) are statistically significantly different ($p < 0.05$; ANOVA). The two-stage linear step-up procedure of Benjamini, Krieger and Yekutieli was used to control the false discovery rate (FDR) over multiple testing (n = 24) with statistical significance accepted at $q < 0.05$. PE and Hex1Cer did not meet the threshold for significance when correcting for multiple testing. Post-hoc testing revealed significant differences between WT and LacQ140 animals, highlighted in green ($p < 0.05$; Tukey's HSD). Subclasses significantly different by ANOVA but with no difference between WT and LacQ140 animals are highlighted in grey ($p < 0.05$; Tukey's HSD). In some cases, lowering of m*Htt* in LacQ140 animals led to significant recovery of lipid abundance levels comparable to WT animals. This is indicated by * in the *adjusted p-value (q)* column ($p < 0.05$; Tukey's HSD).

Table 3. 12-month-old LacQ140 mice surveyed by lipidomics

Category	Subclass	% Total Lipid	Species Detected	ANOVA p-value	Adjusted p-value (q) n = 29
Glycerophospholipids	PC	48.129	160	0.4243	0.4627
	PE	18.895	119	0.5653	0.5372
	PS	3.748	25	0.46	0.4627
	PI	1.881	34	0.0086	0.0338
	MePC	0.932	15	0.7552	0.6329
	PA	0.107	9	0.0025	0.0184
	BisMePA	0.058	6	0.2812	0.3647
	PG	0.052	4	0.859	0.6765
	BisMePS	0.022	2	0.0001	0.0022
	PIP2	0.016	3	0.0161	0.0394
	BiotinylPE	0.002	1	0.0225	0.0451
	LPE	0.544	4	0.0127	0.035
	LPC	0.409	7	0.2805	0.3647
	LPS	0.022	2	0.0817	0.1287
Glycerolipids	TG	1.404	72	0.0002	0.0022
	DG	0.427	59	0.6614	0.5834
	MGMG	0.217	6	0.0497	0.0887
	MGDG	0.181	5	0.0214	0.0451
Sphingolipids	Hex1Cer	13.465	104	0.4617	0.4627
	SM	3.770	36	0.3243	0.3973
	CerP	3.235	17	0.0035	0.0193
	Cer	1.565	21	0.4374	0.4627
	ST	0.717	14	0.2176	0.3199
	SPH	0.013	1	0.775	0.6329
	Hex2Cer	0.003	1	0.0112	0.035
Sterol Lipids	ChE	0.089	2	0.9151	0.6958
	ZyE	0.045	3	0.0092	0.0338
Fatty Acyls	AcCa	0.036	2	0.5847	0.5372
Prenol Lipids	Co	0.014	1	0.0523	0.0887
TOTAL	**29**		**735**		

Table 3. 12-month-old LacQ140 mice surveyed by lipidomics. Table shows lipids detected in 12-month-old mice, organized by LIPID MAPS category, then by subclass for each respective category. For each subclass the mean detected lipid intensity across all samples was calculated to indicate overall relative abundance *(% Total Lipid*). The number of individual species detected per subclass is listed under *Species Detected. ANOVA P-value* lists p values calculated from one-way analysis of variance (ANOVA) conducted for each subclass; 12 subclasses (PI, PA, BisMePS, PIP2, BiotinylPE, LPE, TG, MGMG, MGDG, CerP, Hex2Cer, ZyE) are statistically significantly different ($p < 0.05$; ANOVA). The two-stage linear step-up procedure of Benjamini, Krieger and Yekutieli was used to control the false discovery rate (FDR) over multiple testing (n = 29) with statistical significance accepted at $q < 0.05$. MGMG did not meet the threshold for significance when correcting for multiple testing. Post-hoc testing revealed significant no differences between WT and LacQ140 animals ($p < 0.05$; Tukey's HSD). Subclasses significantly different by ANOVA but with no difference between WT and LacQ140 animals are highlighted in grey ($p < 0.05$; Tukey's HSD).

Table 4. Overall comparison of lipidomic results across ages.

Age	# Species detected	# Species different at p<0.05*	# Species different for WT/LacQ140 at p<0.05	# Species different at q<0.05**	# Species different for WT/LacQ140 at q<0.05	# Species recovered with lowering (q<0.05)
6 months	800	9	4	0	0	0
9 months	632	192	72	17	14	14
12 months	735	162	36	72	26	1

***p value for ANOVA; **Adjusted p value determined using Benjamini, Krieger and Yekutieli procedure**

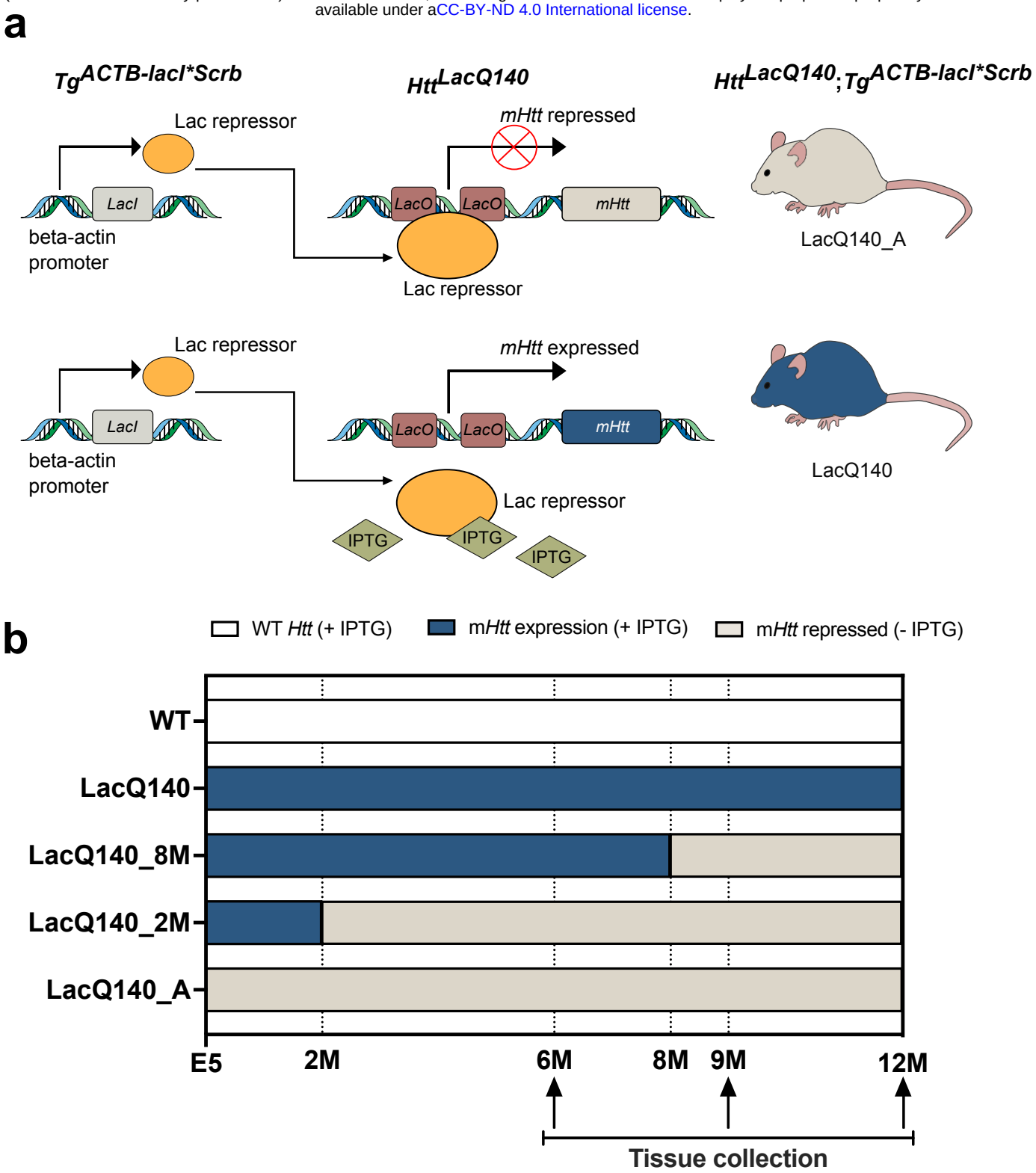

Figure 1. Generation of LacQ140 mice and treatment paradigm (Adapted from Marchionini et al., 2022). **(a)** The *LacO/LacIR*-regulatable HD mouse model (LacQ140) was generated by crossing the $Htt^{LacQ140/+}$ mouse to the $Tg^{ACTB\text{-}lacI*Scrb}$ mouse (Cronin et al., 2001) as previously described (Marchionini et al., 2022). The default state of the LacQ140 mouse is global repression of m*Htt* due to *Lac* Repressor binding to the *Lac* operators. Administration of IPTG starting from embryonic day 5 (E5) interrupts the binding between the *Lac* repressor and operators, resulting in a de-repressed state, and maximal expression of m*Htt* in LacQ140. All WT mice were $Htt^{LacO+/+}$; b-actin-$LacI^{R}$ tg. Illustrations were adapted from Vivek Kumar (10.5281/zenodo.4072320) and Heath Robinson (10.5281/zenodo.7058520), https://scidraw.io. **(b)** Mice were fed *ad libitum*; the lactose analog IPTG was provided in drinking water (at 10mM) which de-represses the *LacQ140* allele and keeps normal m*Htt* expression. During embryonic development, m*Htt* expression levels were maintained at normal levels by administering IPTG to pregnant dams starting at embryonic day 5 (E5). IPTG was continuously administered to WT mice. IPTG was administered always (m*Htt* always expressed, LacQ140), withdrawn at 8 months (m*Htt* repressed beginning at 8 months, LacQ140_8M), withdrawn 2 months (m*Htt* repressed beginning at 2 months, LacQ140_2M), or never administered (m*Htt* always repressed, LacQ140_A). Tissue for each group was collected at 6, 9, and 12 months of age.

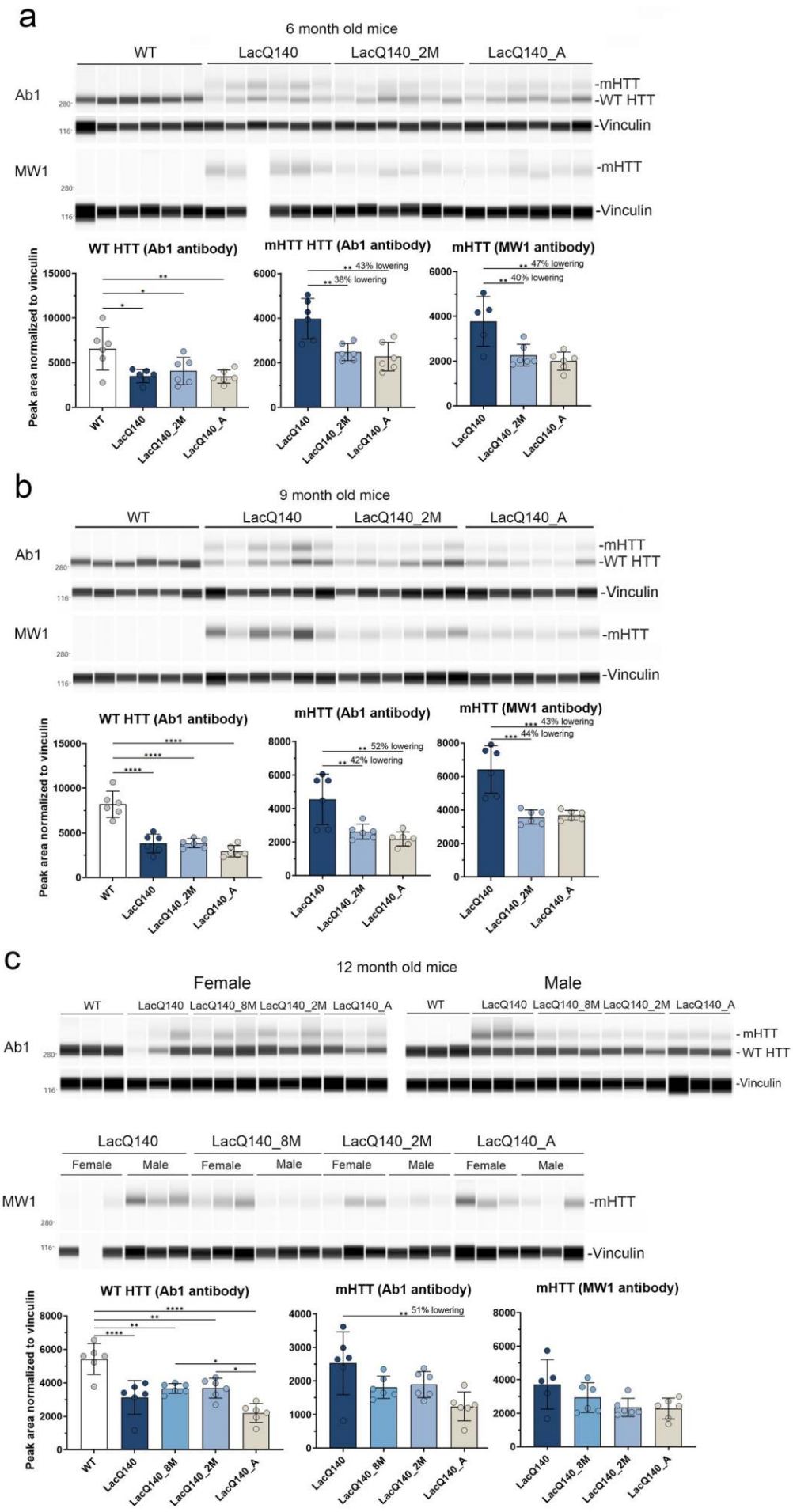

Figure 2. Analysis of mHTT protein levels in crude homogenates of 6, 9 and 12 months old mice. HTT levels were analyzed by capillary immunoassay on equal amounts of protein (0.6 μg) using anti-HTT antibody Ab1 and anti-polyQ antibody MW1 (**a**). Peak area analysis performed using Compass software in 6-month-old mice shows a significant decrease in WT HTT as detected with Ab1 in all LacQ140 mice compared to WT mice. mHTT levels are significantly lower in LacQ140_2M and LacQ140_A as detected with both Ab1 and MW1 compared to LacQ140 (**a**, Ab1: -38% and -43% respectively; MW1: -40% and -47% respectively; **p<0.01, One-way ANOVA with Tukey's multiple comparison test, N=6). Peak area analysis in 9-month-old mice shows a significant decrease in WT HTT as detected with Ab1 in all LacQ140 mice compared to WT mice. mHTT levels are significantly lower in LacQ140_2M and LacQ140_A, as detected with both Ab1 and MW1, compared to LacQ140 (**b**, Ab1: -42% and -52% respectively; MW1: -44% and -43% respectively; **p<0.01, ***p<0.001, One-way ANOVA with Tukey's multiple comparison test, N=6). Peak area analysis in 12-month-old mice shows a significant decrease in WT HTT as detected with Ab1 in all LacQ140 mice compared to WT mice. WT HTT was significantly lower in LacQ140_A compared to LacQ140_8M and LacQ140_2M mice. MHTT levels are significantly lower in LacQ140_A mice, as detected with Ab1, compared to LacQ140 (**c**, Ab1: -51%, **p<0.01, One-way ANOVA with Tukey's multiple comparison test, N=6).

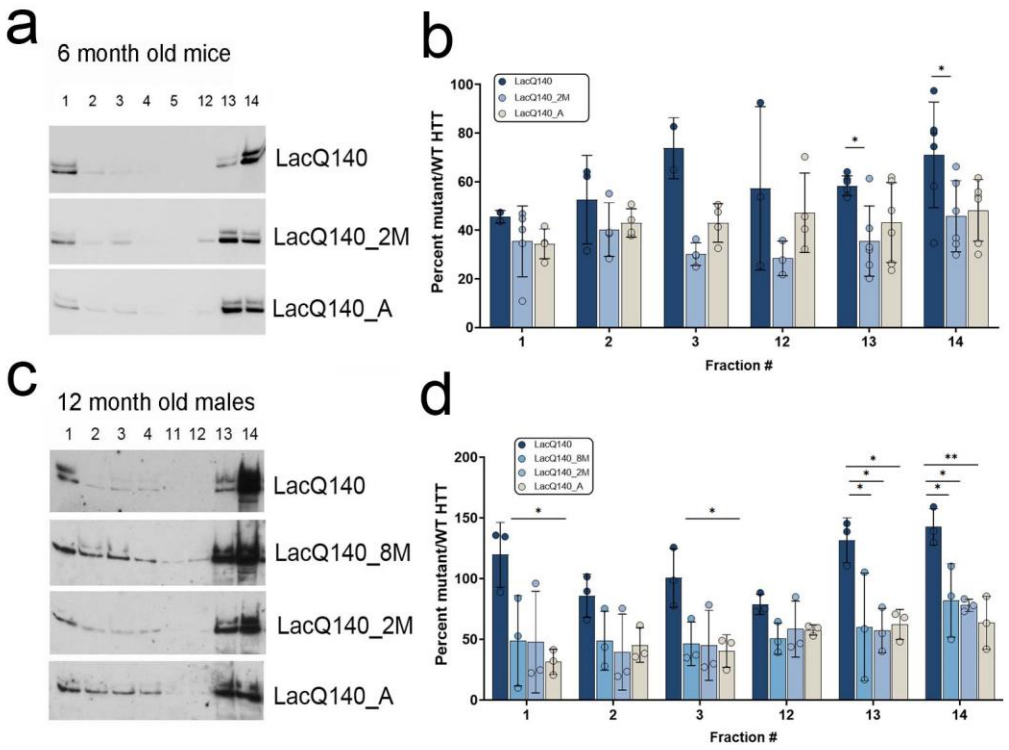

Figure 3. Effects of m*Htt* lowering on the subcellular distribution of WT and mHTT protein by density gradient ultracentrifugation. Representative western blot images for equal volumes of fractions 1-5 and 12-14 from 6-month-old mice probed with anti-HTT antibody Ab1 are shown in **a**. The remaining images are shown in Supplementary Figure 3c. Total pixel intensity quantification for each band measured using ImageJ software is graphed as average percent mutant/WT HTT ± SD for each fraction (**b**). Since each fraction contains different levels of proteins normally used to control for protein loading, levels of mHTT were normalized to levels of WT HTT which was not repressed/lowered. The ratio mutant/WT HTT is significantly higher in LacOQ140 mice compared to LacQ140_2M in fractions 13 and 14. Representative western blot images for equal volumes of fractions 1-4 and 11-14 from 12-month-old mice probed with anti-HTT antibody Ab1 are shown in **c**. The remaining images are shown in Supplementary Figure 3e. Total pixel intensity quantification for each band is graphed as average percent mutant/WT HTT ± SD for each fraction (**d**). The ratio mutant/WT HTT is significantly higher in LacQ140 compared to LacQ140_8M, LacQ140_2M and/or LacQ140_A mice in fractions 1, 3, 13, and 14. Graphs indicate data in fractions where mHTT was detected in at least 3 mice except LacO_A fractions 1 and 3 where only 2 mice had detectible mHTT. *p<0.05, **p<0.01, One-way ANOVA with Tukey's multiple comparison test for each fraction, N=3-6.

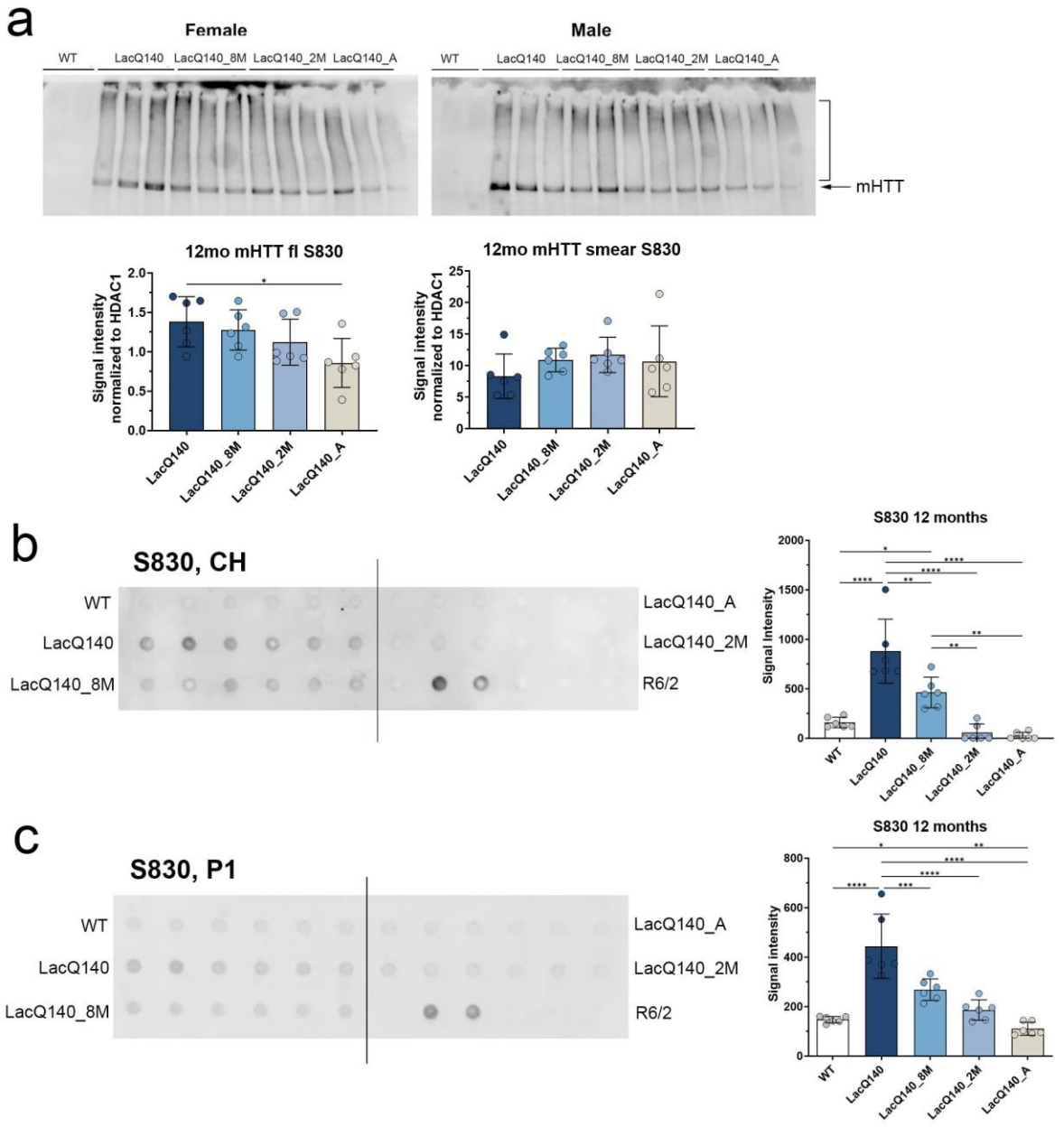

Figure 4. HTT levels in crude homogenates and P1 fractions from WT and LacQ140 mice by western blot and filter trap assay. Equal protein (10 μg) from P1 fractions from 12-month-old LacQ140 and WT mice were analyzed by western blot for HTT levels with anti-HTT S830 (**a**). The S830 antibody detected a smear of HTT signal (bracket) as well as full-length mHTT (arrow). There were significantly lower levels of full length mHTT in the 12-month-old LacQ140_A mice compared to LacQ140 and no changes detected in the HTT smear in all LacQ140 mice (**a**). Filter trap assays of 12-month-old crude homogenates (**b**) and P1 fractions (**c**) were probed with S830 antibody. Each dot represents one animal and each of the 6 dots across equals one group which is labeled on the left and right sides. There are 2 dots for the lysates from R6/2 HD mice which have a highly expressing transgene for a small fragment of HTT containing a large CAG repeat (180CAGs) and that accumulate numerous aggregates which have been shown to be retained in the assay and were used as a positive control. There was significantly more signal for aggregated mHTT in the 12-month-old LacQ140 mice compared to WT, LacQ140_8M, LacQ140_2M and LacQ140_A mice (**b**, ***p<0.001, One-way ANOVA with Tukey's multiple comparison test, n=6). In the P1 fractions, there was significantly more signal for aggregated mHTT detected with S830 antibody in the 12-month LacQ140 mice compared to WT, LacQ140_8M, LacQ140_2M and LacQ140_A mice and in LacQ140_8M compared to WT and LacQ140_A mice (**c**, *p<0.05, **p<0.01, ***p<0.001, One-way ANOVA with Tukey's multiple comparison test, n=6).

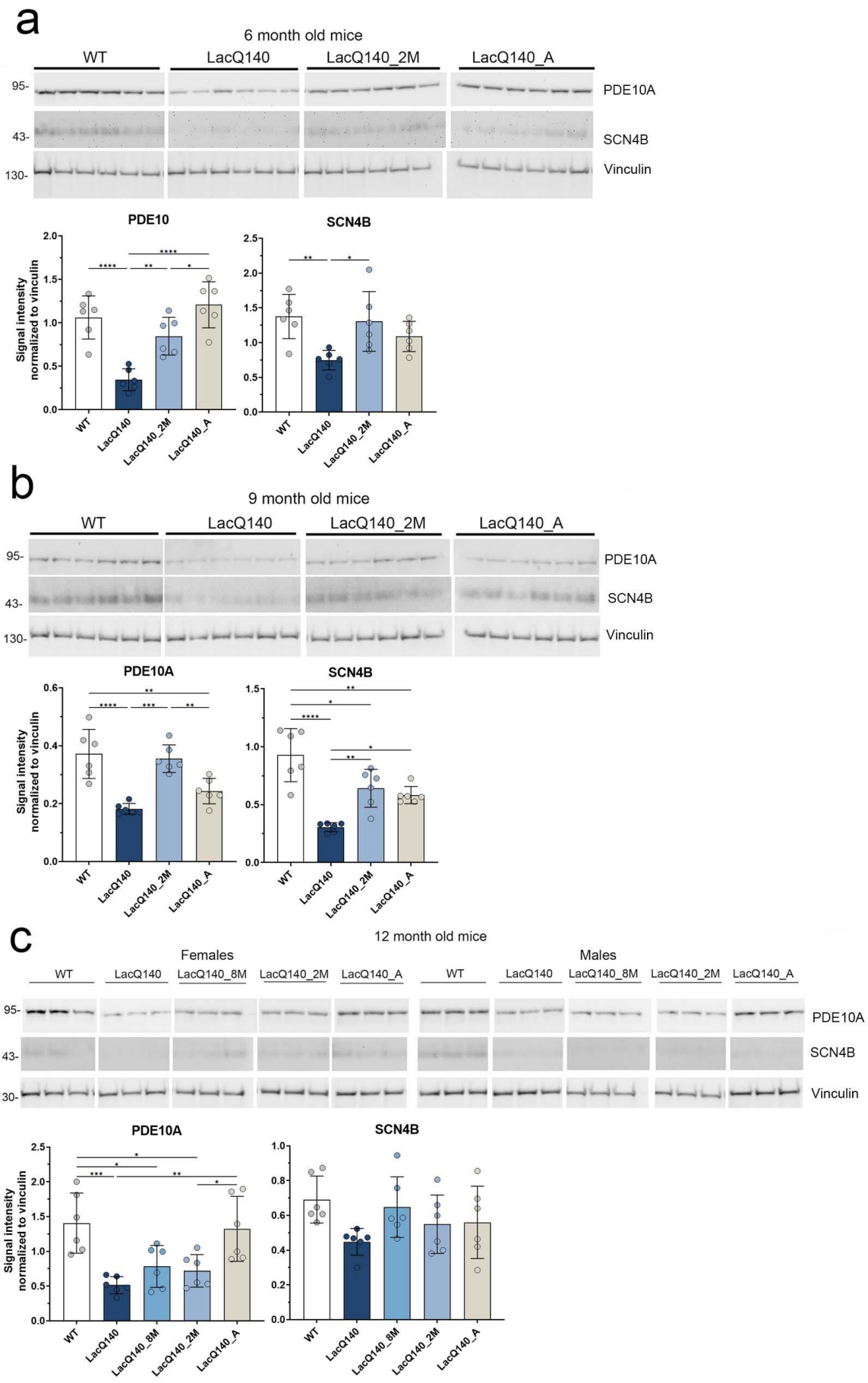

Figure 5. Duration of m*Htt* lowering in 6, 9 and 12 months old LacQ140 mice affects levels of PDE10A and SCN4B.
PDE10A and SCN4B levels were analyzed by western blot on equal amounts of protein (10 μg). Total pixel intensity quantification for each band using ImageJ software in 6-month-old mice shows a significant decrease in PDE10A levels in LacQ140 compared to WT mice. There is an increase in PDE10A levels in LacQ140_2M and LacQ140_A mice compared to LacQ140 and no change from WT mice (**a,** *p<0.05, **p<0.01, ***p<0.001, One-way ANOVA with Tukey's multiple comparison test, n=6). There is a significant decrease in SCN4B levels in LacQ140 compared to WT mice and a significant increase back to WT levels in LacQ140_2M mice.

Total pixel intensity quantification in 9-month-old mice shows a significant decrease in PDE10A levels in LacQ140 compared to WT mice. There is an increase in PDE10A levels in LacQ140_2M compared to LacQ140 and no change from WT mice (**b,** **p<0.01, ***p<0.001, One-way ANOVA with Tukey's multiple comparison test, n=6). There is a significant decrease in SCN4B levels in LacQ140 compared to WT mice. There is a significant increase in SCN4B levels in LacQ140_2M and LacQ140_A mice compared to LacQ140 but significantly lower than in the WT mice (**b,** *p<0.05, **p<0.01, ***p<0.001, One-way ANOVA with Tukey's multiple comparison test, n=6).

Total pixel intensity quantification in 12-month-old mice shows a significant decrease in PDE10A levels in LacQ140, LacQ140_8M and LacQ140_2M compared to WT mice. There is an increase in PDE10A levels in LacQ140_A mice compared to LacQ140 and LacQ140_2M and no change from WT mice (**c,** *p<0.05, **p<0.01, ***p<0.001, One-way ANOVA with Tukey's multiple comparison test, n=6). There are no changes in SCN4B levels in any of the LacQ140 or WT mice.

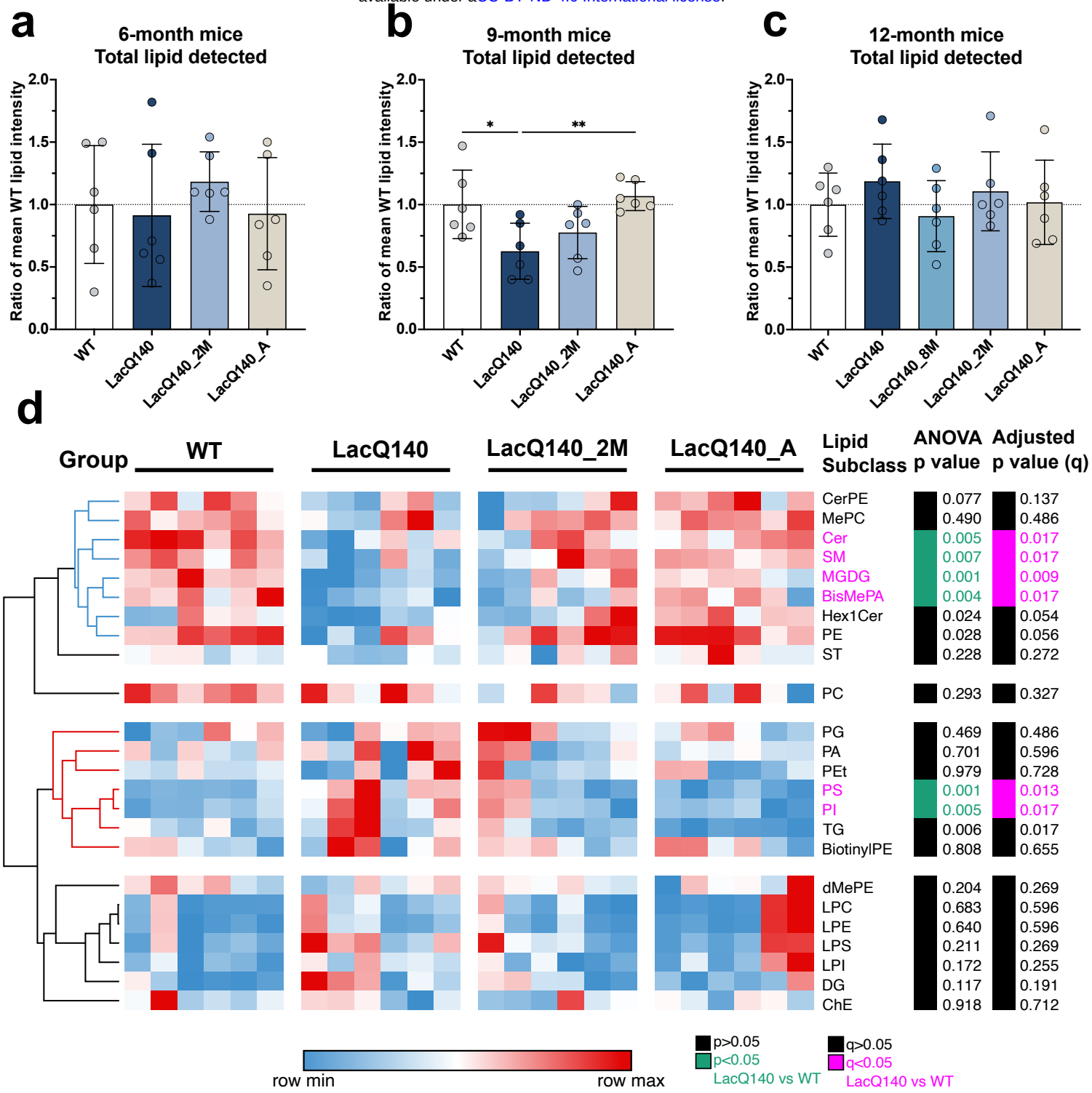

Figure 6. Analyses of lipids in crude homogenates from WT and LacQ140 caudate-putamen by mass spectrometry.
(a-c) Relative levels of total lipids at 6, 9 and 12 months for LacQ140 treatment groups are expressed as a ratio of WT for each timepoint. Lipid intensities for each animal were summed, with each plotted point representing the total lipid intensity detected for one mouse, standardized to the mean WT lipid intensity. At 6 months (a), there was no significant difference in relative total lipid intensity between any group (One-way ANOVA with Tukey's multiple comparisons test, n=6). At 9 months (b), a significant decrease in relative total lipid intensity occurred in LacQ140 mice compared to WT mice and levels normalized in the LacQ140_A mice (*p<0.05, **p< 0.01, One-way ANOVA with Tukey's multiple comparison test, n=6). At 12 months (c), there was no significant difference between any group (One-way ANOVA with Tukey's multiple comparisons test, n=6). **(d)** Heatmap depicts the entire lipid profile for WT, LacQ140, and treatment groups at 9 months. Each column represents data from one animal. Hierarchical clustering was performed across all lipid subclasses (rows) using the one minus Pearson correlation distance metric. Lipid intensity values are assigned to colors based on the minimum (blue, low relative expression) and maximum (red, high relative expression) values for each independent row. The blue cluster identified lipid subclasses that trended to move lower in LacQ140 mice with full m*Htt* expression and recovered up with m*Htt* lowering. The red cluster identified lipid subclasses that trended to move higher in LacQ140 mice with full m*Htt* expression and recovered down with m*Htt* lowering. Clusters in black showed no changes. For each lipid subclass, the ANOVA p-value is displayed to the right with the green annotation indicating lipid subclasses significantly changed between LacQ140 and WT mice (p<0.05, One-way ANOVA with Tukey's multiple comparison test, n=6). The FDR adjusted p-value (q) is displayed to the right of the ANOVA p-value with the pink annotation indicating each lipid subclass significantly changed between LacQ140 and WT mice (q <0.05, two-stage linear step-up procedure of Benjamini, Krieger and Yekutieli, n=24 lipid subclasses).

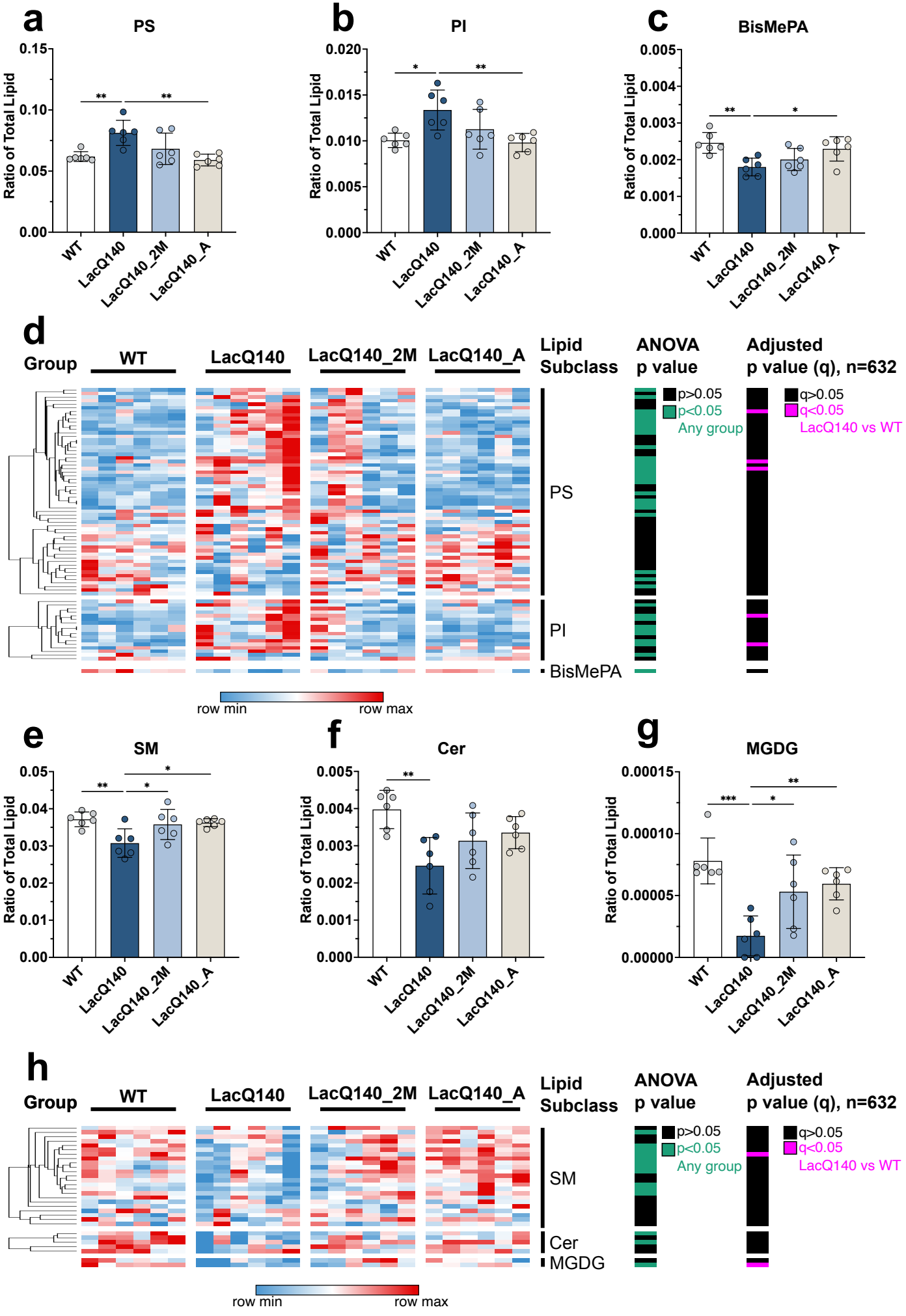

Figure 7. Dysregulated lipid subclasses at 9 months and recovery with partial lowering of mutant huntingtin.
Graphs show relative intensities for indicated lipid subclasses expressed as a ratio of total lipid intensity per sample for each genotype or treatment group. Plotted values represent summed lipid subclass intensity standardized to total amount of lipid detected in the same sample. Significant increases in the LacQ140 mice compared to WT mice were measured for glycerophospholipid subclasses **(a)** phosphatidylserine (PS), **(b)** phosphatidylinositol (PI), and a significant decrease was measured in **(c)** Bis-methyl phosphatidic acid (BisMePA). These changes were corrected with early lowering of m*Htt* (LacQ140_A) (*N* = 6 mice per group, One-way ANOVA with Tukey's multiple comparison test *$p < 0.05$, **$p < 0.01$). **(d)** Heatmap shows the individual lipid species that comprise each glycerophospholipid subclass. Each column represents data from one animal. Hierarchical clustering was performed across individual lipid species in each subclass using the one minus Pearson correlation distance metric. Lipid intensity values are assigned to colors based on the minimum (blue, low relative expression) and maximum (red, high relative expression) values for each independent row. The ANOVA p-value column indicates individual species significantly changed between any group in green and unchanged individual species in black (p<0.05, One-way ANOVA with Tukey's multiple comparison test, n=6). The adjusted p-value (q) column indicates annotation indicates individual lipid species significantly changed between LacQ140 and WT mice in pink: 3 species PS, 2 species PI (q <0.05, two-stage linear step-up procedure of Benjamini, Krieger and Yekutieli, n=632 lipid species). Significant decreases in LacQ140 mice compared to WT mice were measured for sphingolipid subclasses **(e)** sphingomyelin (SM), **(f)** ceramide (Cer), and the glycerolipid subclass **(g)** monogalactosyl diacylglycerol (MGDG). Lowering m*Htt* in both groups (LacQ140_2M and LacQ140_A) corrected levels of SM and MGDG, whereas lowering m*Htt* did not restore levels of Cer (*N* = 6 mice per group, One-way ANOVA with Tukey's multiple comparison test * $p < 0.05$, **$p < 0.01$, ***$p < 0.001$). All subclasses **(a-c, e-g**) had q values<0.05 after correction using the two-stage linear step-up procedure of Benjamini, Krieger and Yekutieli (n=24 subclasses). **(h)** Heatmap shows the individual lipid species that comprise each subclass. Each column represents data from one animal. Hierarchical clustering and color mapping is described above and in methods. The ANOVA p-value column indicates individual species significantly changed between any group in green and unchanged individual species in black (p<0.05, One-way ANOVA with Tukey's multiple comparison test, n=6). The adjusted p-value (q) column indicates annotation indicates individual lipid species significantly changed between LacQ140 and WT mice in pink: 1 species SM, 1 species MGDG (q <0.05, two-stage linear step-up procedure of Benjamini, Krieger and Yekutieli, n=632 lipid species).